Mechanisms for Extreme Precipitation Changes in a Tropical Archipelago

Daniel Argüeso, A. Di Luca, Nicolas Jourdain, R. Romero, V. Homar

Journal of Climate

Mechanisms for extreme precipitation changes in a tropical archipelago

--Manuscript Draft--

Manuscript Number:	JCLI-D-21-0224
Full Title:	Mechanisms for extreme precipitation changes in a tropical archipelago
Article Type:	Article
Corresponding Author:	Daniel Argüeso University of the Balearic Islands Palma, Baleares SPAIN
Corresponding Author's Institution:	University of the Balearic Islands
First Author:	Daniel Argüeso
Order of Authors:	Daniel Argüeso
	Alejandro Di Luca
	Nicolas C. Jourdain
	R. Romero
	V. Homar
Abstract:	The Maritime Continent is one of the most challenging regions for atmospheric models. Processes that modulate deep convection are poorly represented in models, which affects their ability to simulate precipitation features accurately. Thus, future projections of precipitation over the region are prone to large uncertainties. One of the key players in modelling tropical precipitation is the convective representation, and hence convection-permitting experiments have contributed to improve aspects of precipitation in models. This improvement creates opportunities to explore the physical processes that govern rainfall in the Maritime Continent, as well as their role in a warming climate. Here, we examine the response to climate change of models with explicit and parameterized convection and how that reflects in precipitation changes. We focus on the intensification of spatial contrasts as precursors of changes in mean and extreme precipitation in the tropical archipelago. Our results show that the broad picture is similar in both model setups, where islands will undergo an increase in mean and extreme precipitation in a warmer climate and the ocean will see less rain. However, the magnitude and spatial structure of such changes, as well as the projection of rainfall percentiles, are different across model experiments. We suggest that while the primary effect of climate change is thermodynamical and it is similarly reproduced by both model configurations, dynamical effects are represented quite differently in explicit and parameterized convection experiments. In this study, we link such differences to horizontal and vertical spatial contrasts and how convective representations translate them into precipitation changes.

Abstract

The Maritime Continent is one of the most challenging regions for atmospheric models. Processes that modulate deep convection are poorly represented in models, which affects their ability to simulate precipitation features accurately. Thus, future projections of precipitation over the region are prone to large uncertainties. One of the key players in modelling tropical precipitation is the convective representation, and hence convection-permitting experiments have contributed to improve aspects of precipitation in models. This improvement creates opportunities to explore the physical processes that govern rainfall in the Maritime Continent, as well as their role in a warming climate. Here, we examine the response to climate change of models with explicit and parameterized convection and how that reflects in precipitation changes. We focus on the intensification of spatial contrasts as precursors of changes in mean and extreme precipitation in the tropical archipelago. Our results show that the broad picture is similar in both model setups, where islands will undergo an increase in mean and extreme precipitation in a warmer climate and the ocean will see less rain. However, the magnitude and spatial structure of such changes, as well as the projection of rainfall percentiles, are different across model experiments. We suggest that while the primary effect of climate change is thermodynamical and it is similarly reproduced by both model configurations, dynamical effects are represented quite differently in explicit and parameterized convection experiments. In this study, we link such differences to horizontal and vertical spatial contrasts and how convective representations translate them into precipitation changes.

Keywords: Maritime Continent, Precipitation, Convection-Permitting, Climate Change, Convective parameterization, Extreme precipitation

1 Introduction

The Maritime Continent (Fig. 1) is the largest archipelago on Earth and one of the most active centers of deep moist convection on the planet. This tropical archipelago comprises thousands of islands of varied sizes and steep topography surrounded by the Indo-Pacific Warm Pool, a region with very high sea surface temperatures. Intense convective processes in the Maritime Continent (MC) shape its precipitation regimes and thus have direct implications locally. However, the scale and magnitude of convection is such that it helps transport large amounts of energy and moisture, modulating global circulation patterns [*Neale and Slingo*, 2003; *Yamanaka et al.*, 2018]. Their intrinsic relationship with phenomena such as the Madden-Julian Oscillation (MJO) [*Birch et al.*, 2016] and the Walker Circulation-ENSO [*Qian et al.*, 2010] are key examples of the interaction across-scales that occur in the Maritime Continent.

The region has proven very challenging in terms of understanding and modelling precipitation characteristics and the associated physical processes. Despite the importance of the region at multiple scales, Global Climate Models fail to capture key features of the Maritime Continent such as the MJO propagation [*Peatman et al.*, 2014; *Ling et al.*, 2019] and the diurnal cycle of rainfall [*Baranowski et al.*, 2019], largely due to their coarse resolution. In fact, even the most recent generation of GCMs (CMIP6) still show substantial biases in tropical precipitation [*Fiedler et al.*, 2020]. As a result, even though the CMIPs multi-model means suggest increases in rainfall over the region (CMIP5: *Jourdain et al.* [2013] and Supplementary Figure S1; CMIP6: *Wang et al.* [2020]), individual GCMs strongly disagree in the sign of rainfall changes [*Jourdain et al.*, 2013; *Narsey et al.,* 2020].

Regional Climate Models (RCMs), which operate at higher spatial resolution, have contributed to improve our understanding and simulation of the mechanisms underlying rainfall in the Maritime Continent [*Vincent and Lane*, 2018; *Ruppert and Zhang*, 2019; *Li et al.*, 2020] through better representation of fine-scale processes (i.e., sea-breeze, gravity waves, interaction across scales, air-ocean fine-scale interactions). However, RCMs are still prone to substantial errors, partly originated from the interaction between the convective representation and the land-sea contrasts [*Birch et al.*, 2015; *Vincent and Lane*, 2017; *Im and Elthair*, 2018]. Models that explicitly represent convection bring improvements in the simulation of the precipitation diurnal cycle but produce unrealistic precipitation over steep topography [*Argüeso et al.*, 2016; 2020], misrepresent the amplitude of the diurnal cycle [*Hassim et al.*, 2016, *Argüeso et al.* 2020] or introduce errors in the rainfall modulation by the MJO phase [*Vincent and Lane*, 2017; *Wei et al.*, 2020]. The challenges posed to models by convective processes in the MC have attracted much attention in the recent years because of their central role in the climate at multiple scales. A perfect example of this interest is the international initiative "Years of the Maritime Continent" (YMC Phase 1 2017-2020, *Yoneyama and Zhang* [2020]), aimed at coordinating international modelling and observational efforts to advance our understanding of the MC weather-climate systems, and to improve the representation of convective processes and precipitation in models.

Precipitation in the Maritime Continent tends to concentrate over the islands [*Qian*, 2008], where rainfall is characterized by a strong diurnal cycle that most models struggle to capture. As described by *Ruppert and Chen* [2020], the "island rainfall enhancement" effect and the land precipitation diurnal cycle are ultimately linked to differences between land and ocean in surface heat capacity and surface energy fluxes. They also show that the diurnal cycle of solar radiation governs mesoscale circulations (i.e., land-sea and mountain-valley breezes), which in turn fuel the

91 convective development, help organize deep convection into mesoscale convective systems and
92 recharge the convective instability required for intense rainfall rates. Local steep topography
93 further contributes to organize convection by exciting and coupling with gravity waves and, in
94 certain situations, to reinforce it by inducing orographic lifting. These convective systems then
95 propagate offshore, assisted by gravity waves, reversed breezes (land breeze) and cold pools
96 [*Ruppert and Zhang*, 2019; *Yang et al.*, 2020], which together produce a diurnal cycle over water
97 that peaks between night and early morning, albeit generally weaker than over land. Therefore,
98 rainfall features in the MC strongly depend on local factors such as land-ocean contrasts,
99 mesoscale circulations, moisture convergence, intense convective instability, and topography.
100 In the context of climate change, we expect horizontal and vertical warming contrasts that may
101 induce changes in the intensity and spatial distribution of precipitation. For example, differences
102 in warming rates between continents and ocean can alter mesoscale circulations [*Joshi et al.*, 2007]
103 and vertical warming contrasts can modify atmospheric stability [*Wang et al*., 2020], which will
104 likely affect rainfall in the Maritime Continent. At the ocean basin scale, thermal contrasts will
105 also play a key role in defining future changes of the Walker Circulation [*Yim et al.*, 2017] –and
106 hence in the El Niño-Southern Oscillation–, which ascending branch is anchored to the Maritime
107 Continent and likely modulated by the "island rainfall enhancement" effect [*Ruppert and Chen*,
108 2020]. At continental and seasonal scales, monsoons will be also intensified due to enhanced
109 thermal contrasts [*Seth et al.*, 2019], which may redistribute precipitation.
110 In the Maritime Continent, *Lambert et al.* [2017] did not find a consistent shift of rainfall from
111 ocean to land due to warming, as opposed to other tropical regions (i.e., Amazonia). *Bony et al.*
112 [2013] also identified land-sea thermal contrasts as having an important role in modifying tropical
113 rainfall patterns over land, although they deemed the dominant factor in tropical overturning

114 circulation to be the higher CO_2 concentrations and the resulting radiative imbalance in the
115 atmosphere. However, all these changes were established using Global Climate Models (GCMs),
116 which have serious difficulties in representing crucial features of the Maritime Continent rainfall
117 [*Jourdain et al.,* 2013; *Schiemann et al.*, 2013; *Baranowski et al.*, 2019; *Yang et al.*, 2020]. Recent
118 studies have generated future climate projections using RCMs [*Supari et al.,*2020*; Tangang et al.,*
119 2020] and found that both increases and decreases in land precipitation over areas of the MC were
120 plausible, depending on the region and the season examined. Yet, the physical mechanisms driving
121 such changes have not been explored.

122 Therefore, the use of higher-resolution models to better understand the mechanisms driving
123 future changes in precipitation over the region is still necessary. Despite some errors that persist
124 in high-resolution models, experiments that explicitly resolve convection are especially beneficial
125 in coastal areas, regions of complex topography and locations with frequent and intense deep
126 convection [*Prein et al.*, 2015; Lucas-Picher et al. 2021], all of which apply to the Maritime
127 Continent. In this study, we use a model at convection-permitting scales to investigate the response
128 of rainfall to a warming climate. For the first time, we examine future climate information at
129 convection-permitting scales in the entire Maritime Continent and determine the different response
130 of rainfall extremes to climate change in parameterized and explicit convection experiments. We
131 also conducted a novel analysis of the role of warming spatial contrasts, land-sea breeze
132 circulations and modified atmospheric stability in modulating this response. We expect that land-
133 sea thermal contrast changes will affect breeze circulations, and vertical differences in the response
134 to global warming will modify vertical profiles and stability. In combination, they will have
135 implications for future climate precipitation regimes in the region. Since the interactions between
136 convection and the environment are represented differently in explicit and parameterized

convection models, precipitation responses to climate change will likely differ between these models too. In view of this possibility and the expectations around convection-permitting models for future projections [*Fosser et al.*, 2020; *Prein et al.*, 2020; Lucas-Picher et al. 2021], we explore the rainfall response to increased temperature in both explicit and parameterized convection experiments at very high resolution.

The rate at which precipitation responds to surface temperature changes is known as precipitation scaling [*Trenberth*, 1999; *Held and Soden*, 2006] and has two main components: dynamical and thermodynamical (see Box 11.1 in *Seneviratne et al.* [2021]). In the past, also the co-variational term was explored [*Bony et al.* 2004]. The thermodynamical component is linked the Clausius-Clapeyron relationship –increased atmospheric water-holding capacity with temperature– and is a primary mechanism for climate-scale precipitation changes. Under climate change conditions, this should contribute to more intense precipitation rates, particularly for extremes [*Dobrinski et al.* 2018]. The dynamical component includes changes in large-scale circulation patterns that determine the supply of moisture and in local circulations that contribute to vertical motions. The intensification of sea-breeze, atmospheric instability and convective processes is framed in the latter group (i.e., local circulations). Here, we focus on the role of local circulations to explain the spatial patterns of precipitation changes, which is related to the dynamical part. However, we also explore the contribution of thermodynamical changes to provide a comprehensive picture. We examine the separate contribution of thermodynamical and dynamical mechanisms to intense precipitation changes in the region and we identify differences between parameterized and explicit convection models in this context.

2 Methods

2.1 Model and present-climate experiments

In this study, we use the Weather Research and Forecasting (WRF) Model v3.9.1 [*Skamarock et al.*, 2008] to simulate the atmosphere over the Maritime Continent and investigate rainfall patterns under climate change conditions. The model was run at 4-km spatial resolution over a domain covering 5916 km by 2556 km (1479 by 639 grid points) in the Maritime Continent and resolving the vertical with 50 hybrid coordinate levels. The experiments span three consecutive austral summers (1st November to 1st March; 2013-2014, 2014-2015 and 2015-2016), each preceded by a 10-day spin-up period (22nd October – 31st October) that was discarded in the analysis. The analysis period covers the wet season for most of the Maritime Continent and the selected years span both positive and negative phases of the El Niño/Southern Oscillation.

The physical parameterization schemes are among the most widely used options and were chosen according to previous studies over the region [*Li et al.*, 2016; *Argüeso et al.*, 2016; *Vincent and Lane*, 2017]. The setup consists in the WRF single moment 6-class microphysics scheme [WSM6; *Hong and Lim*, 2006], the Yonsei University (YSU) scheme for Planetary Boundary Layer turbulence, the Rapid Radiative Transfer Model scheme for longwave radiation (RRTM), the Goddard scheme for shortwave radiation, the Noah land surface model and the MM5 similarity scheme for the surface layer. In the parameterized convection experiment, the Betts-Miller-Janjic [BMJ; *Betts and Miller*, 1986, 1993; Janjic, 1994] scheme was chosen to represent both deep and shallow convection, while it was turned off for the explicit convection experiment (see *Argüeso et al*. [2020] for additional details on the model configuration). In this framework, clouds are driven by the microphysics parameterization regardless of the convective representation. However, the environmental conditions in the model will depend on the convective representation and thus the

181 microphysics scheme will likely generate different clouds. In the explicit simulations, it is the
182 model equations (dynamical core) that represent convection and its effects on the atmosphere
183 vertical profile. In the parameterized runs, the BMJ scheme does not directly inhibit explicit
184 convection, but it reduces the potential for explicit convection because it removes energy from the
185 atmosphere through the adjustment towards a stable vertical profile. Explicit convection at scales
186 resolved by the model grid is still possible though, especially in environments that favor strong
187 convective processes.

188 Present climate experiments are directly initialized and driven by ERA5 reanalysis [*Hersbach*
189 *et al.* 2020] at circa 0.3° spatial resolution and updated every 6 hours. *Argüeso et al.* [2020] already
190 analyzed these simulations and compared them against satellite-derived products to examine the
191 role of different convective representations and the spatial resolution in representing realistic
192 rainfall features. They concluded that, as opposed to higher resolution experiments, 4-km provides
193 the best estimates of precipitation while maintaining computational and storage costs affordable.
194 This is the upper boundary of the convective grey zone [*Prein et al.,* 2015], a range of spatial
195 resolutions (~4-10km) where explicit and parameterized convection may compete. It is yet unclear
196 whether convection should be parameterized in this range. Thus, it further justifies the analysis of
197 both parameterized and explicit convection setups.

198 ## 2.2 Pseudo Global Warming experiments

199 This study expands the existing set of runs in *Argüeso et al.* [2020] by incorporating Pseudo
200 Global Warming (PGW, [*Schär et al.* 1996]) experiments to examine the response of rainfall to a
201 particular climate change signal. These experiments were built adding the climate change signal
202 obtained from a global climate multi-model ensemble from the Coupled Inter-comparison Model
203 Project Phase 5 (CMIP5). We calculated the seasonal cycle of all variables ingested by the model

(i.e., wind components, humidity, geopotential height and temperature at pressure levels; and 2-m dew-point temperature, 2-m temperature, 10-m wind components, surface pressure, mean sea level pressure, and sea surface temperature) for historical (1989-2009) and future (2080-2100) climate experiments from 33 GCMs (Supplementary material). We computed the climate change signal for each calendar month, each variable, and each model, and interpolate them to a common 0.72° grid to calculate a multi-model mean climate change signal. These monthly changes are linearly interpolated in time to 6-hourly intervals and nearest-neighbor interpolated to the ERA5 grid. Then they are added to ERA5 to create the initial and boundary conditions to drive WRF under a synthetic future climate scenario. The PGW method has been previously evaluated in a "perfect model approach" with satisfactory results [*Yoshikane et al.,* 2012; *Donat-Magnin et al.,* 2021] and was applied in a wide range of studies from tropical cyclones [*Chen et al.,* 2020] to ice sheets [*Donat-Magnin et al.,* 2021].

The future climate change signal is here represented by the Representative Concentration Pathway 8.5 (RCP8.5 scenario). We chose this high-emission scenario to examine the impact of a marked climate change signal on the Maritime Continent, but this choice does not imply any assumptions on its likeliness.

Even though this experiment set up does not constitute a rigorous future climate projection and thus has limitations, it offers numerous advantages. While runs are not long enough to be completely representative of the climate, their duration is a very good reason to force future climate runs with climatological anomalies from the GCMs multi-model ensemble (MMM). This way, our results are less dependent on the interannual variability produced by individual models for specific years. Furthermore, it is often argued that changes projected by the MMM are in general more credible than projections produced by individual models [*Knutti et al.,* 2010]. In addition, CMIP5

models' biases are stationary even under strong climate changes [*Krinner and Flanner, 2*018], hence this method partly overcomes the biases in the climate states produced by individual models. The MMM estimates are still subjected to biases, such as the Sea Surface Temperature warming patterns that require complex bias-correction methods [*Dutheil et al.*, 2020], but the same applies to direct downscaling of individual highly biased GCMs. The PGW method includes the thermodynamical effects produced by a given climate change signal and some dynamical features. For example, it considers the mean change in the large-scale dynamics because the geostrophic balance is linear. However, it misses changes in the structure and variability of circulation patterns, as well as some non-linear large-scale dynamics and variability. These include phenomena such as MJO or ENSO, some of which may undergo frequency changes in the future [*Cai et al.,* 2018]. Another potential limitation is that non-stationary biases that may be shared by CMIP5 models are not removed with the multi-model mean. It is important to note that these features can affect the spatial patterns of precipitation changes in our experiments.

Overall, the method constitutes an interesting, efficient, and solid approach to quantify the response of the climate change system to plausible future conditions. It also brings the analysis down to the physical-process level at feasible computational costs, especially considering the demands of convection-permitting experiments at continental scales. In this study, we refer to the PGW simulations as "future" experiments for clarity reasons. Changes projected by the selected multi-model ensemble over the Maritime Continent are shown in the supplementary material (Supplementary Figure S1) for temperature, wind, precipitation, and integrated water vapor.

2.3 Scaling calculation

We first calculate the scaling of extreme precipitation with temperature directly from the model outputs. To further understand the underlying mechanisms, we also calculate changes in

precipitation extremes using the physical scaling diagnostic described in *O'Gorman and Scheneider* [2009b], which estimates precipitation rates from vertical profiles of vertical pressure velocity, temperature, and pressure. This methodology is usually applied to high-percentile precipitation events by selecting times when they occur. It expresses the precipitation rate during an extreme event at each grid point as:

$$P_e \sim -\left\{\omega_e \left.\frac{dq_s}{dp}\right|_{\theta^*,T_e}\right\} \qquad \text{Eq. 1}$$

Where P_e is the precipitation amount during an extreme event, ω_e is the corresponding vertical pressure velocity, $\{\cdot\}$ is a mass-weighted integral over the troposphere, and the remainder is the vertical derivative of the saturation specific humidity q_s at constant saturation equivalent potential temperature θ^* (i.e., moist adiabatic) and evaluated at the mean temperature T_e during the intense rainfall event (See *O'Gorman and Scheneider* [2009b] for additional details). By comparing estimates from present- and future-climate experiments, it is possible to approximate the full precipitation scaling for extremes, which aggregates the effects of thermodynamic and dynamic processes.

Following *Pfahl et al.* [2017], we can decompose changes in heavy rainfall into thermodynamic and dynamic contributions. To calculate the separate effect of thermodynamic processes, we ignore changes in the vertical profile of ω_e and we use instead the time-average from present climate experiments calculated only for extreme precipitation hours ($\overline{\omega_{e\_present}}$). The new heavy rainfall estimates (P_{e_thermo}, Eq. 2) will be due to changes in the vertical derivative of q_s only. The dynamic contribution (P_{e_dyn}, Eq.3) is calculated by subtracting the thermodynamic scaling (Eq 2) from the full scaling (Eq. 1).

$$P_{e\_thermo} \sim -\left\{\overline{\omega_{e\_present}} \left.\frac{dq_s}{dp}\right|_{\theta^*,T_e}\right\} \quad \text{Eq. 2}$$

$$P_{e\_dyn} = P_e - P_{e\_thermo} \quad \text{Eq. 3}$$

In this study, we apply for the first time this diagnostic to convection-permitting experiments and hourly model outputs to disentangle the contribution of thermodynamic and dynamic processes and explain possible deviations from the Clausius-Clapeyron relationship at very high spatiotemporal scales. Prior to applying the scaling, we horizontally smoothed the vertical pressure velocity (ω_e) – not the vertical derivative of q_s – using a gaussian filter with a standard deviation of 20 km. Reasons for this include: 1) to reduce the effect of downdrafts produced by intense rainfall within the convective cell and characterize the environment producing the extreme episode, 2) to filter out the influence of single-cell storms that models may generate at these scales [*Murata et al.,* 2017a] and 3) to better match the scales previously used with this method (~100 km) [*Pfahl et al.*, 2017]. Scaling was also calculated without any prior spatial smoothing.

3 Results

3.1 Precipitation changes in explicit and parameterized convection models.

In this section, we analyze changes in mean precipitation as simulated by the parameterized (PA) and explicit (EX) convection experiments. We compare present and future experiments over three consecutive austral summers (NDJF) and calculate changes relative to present-climate values ([future-present]*100/present). Mean precipitation changes show a prominent contrast between a net increase over land and a decrease over the ocean (Fig. 2). Both model configurations simulate a domain-average decrease in mean precipitation (-13.3% for PA and -6.2% for EX), probably

because they are driven by the same boundary conditions, which exert control over the large-scale dynamics. The MMM of the CMIP5 ensemble used here to create the PGW scenario project a slight increase in the domain-average rainfall (4.9%), but precipitation is a model prognostic variable and is not used to generate the boundary conditions. While this difference in the sign of changes may seem contradictory, the link between the large-scale conditions and precipitation in models is complex. Factors that contribute to this disparity include differences in the spatial scale (grid-averaging effects), in the efficiency of convective schemes, in the response of convective schemes to environmental changes and in surface evapotranspiration. Furthermore, the CMIP5 ensemble projects a wide range of possible changes over the domain (between -16.6% and 19.8%). Despite these differences and the divergence across CMIP5 models [*IPCC*, 2013; and Supplementary Figure S1], the ensemble consistently projects larger increases over land than over the ocean, which is coherent with our results (Fig. 2).

Both our experiments produce an increase in rainfall over land (4.3% PA; 5.0% EX) and a decrease over the ocean (-20.2% PA; -12.7% EX). Narrow waters in between islands and coastal areas are notable exceptions to this general response. Thus, according to our experiments, a warmer atmosphere would generate more rainfall over land in the Maritime Continent, although the spatial variability is large over both land and ocean (Fig. 2e). Changes are similar across all three austral summers in the PA runs and results from one year deviate from the other two in the EX run (Fig. 2e and Supplementary Figure S2). Altogether, this provides confidence on the robustness of the results.

The spatial pattern of precipitation changes is broadly similar in both experiments, but there are features in the response that differ between the two. Firstly, the magnitude of changes: PA produces larger decreases of rainfall over the ocean. Secondly, EX experiments are spatially

noisier and so is the response to warming. This is partly explained by the length of the simulations, but PA is spatially much smoother, which suggests that the noise is inherent to how convective processes are represented. In fact, changes in EX shows a larger year-to-year variability than PA under the same large-scale conditions (Fig. 2e). This contrast is relevant because the next generation of climate projections will shift towards convection-permitting models [*Prein et al.,* 2015, 2020], which may produce less spatially homogeneous projections if they behave like our model. None of the two model projections can be deemed more likely than the other because their relative performance varies depending on the metric analyzed [*Argüeso et al.,* 2020]. However, explicit convection brings increased realism of precipitation features often misrepresented in models such as the diurnal cycle and its coupling with the land-sea breeze [*Birch et al.*, 2015; *Argüeso et al.*, 2020].

In addition to mean precipitation, we analyze the model extreme precipitation response to a climate change signal and quantify the role of convective representation in that response (Fig. 3). We characterize changes in precipitation events through a range of percentiles (50^{th} to 99.9^{th}) and focus on the upper tail of the distribution (95^{th}, 98^{th}, 99^{th} and 99.9^{th} percentiles). The statistical significance of changes was tested at the 90% confidence level using a bootstrapping approach based on resampling with replacement following *Contractor et al.* [2018, 2021]. For each grid point, we concatenated present and future, and resampled the resulting timeseries with replacement under the null hypothesis that there is no change. The same permutation is used for all grid points to preserve spatial dependence in the resampled data. The resampling was done using 12-hour blocks to preserve temporal dependence of events. This assumes independence of rainfall from one 12-hour period to the next, which is supported by the distinct diurnal cycle of rainfall in the region. The diurnal cycle was considered when defining the blocks (06-18UTC and 18-06UTC)

335 so that the rainfall peak at around 5pm LST is not split across two blocks. This approach neglects
336 correlation in rainfall on daily or longer timescales, which could lead to some overestimation in
337 the number of independent samples.

338 We split the resampled timeseries in two equal parts and calculate the change in the percentiles
339 between the two. The process was repeated 1000 times to build a distribution of quantile change
340 ratios between the two, which is normally distributed around 0, and estimate the p-values of the
341 original quantile change ratios. Percentiles were calculated for each grid point and each period
342 (present and future) separately. Percentiles can be calculated using all hourly values [*Schär et al.,*
343 2016] or wet-only values [*Chan et al.,* 2016] depending on the purpose of the analyses. While both
344 may have advantages, we chose the all-hourly values approach because having a fix population of
345 events ensures that: a) changes in each percentile univocally means that events exceeding that
346 percentile (extreme) must change, b) upper percentiles are not affected by changes in light rain
347 frequency, and c) percentiles represent a fixed number of events at all locations, runs and periods.
348 For instance, the upper percentiles we focus on represent circa 433, 173, 87, and 9 hourly events
349 in all grid cells and all experiments. These advantages make our results easier to interpret in the
350 context of this study. Present climate values of these percentiles are provided in the supplementary
351 material (Supplementary Figure S3). Changes in percentiles using wet-only values (>0.1 mm hr^{-1})
352 are shown in Supplementary Figure S4 for comparison with the all-hourly values approach.
353 Changes in wet-only percentiles are comparable to higher percentile changes using all-hourly
354 values. This is because wet-only percentiles characterize a higher section of the rainfall distribution
355 tail. Although changes in wet-only percentiles are affected by changes in the entire distribution of
356 rainfall, the spatial patterns between the two approaches are very similar for very intense

357 precipitation events. They both show a land-sea contrast. Differences between PA and EX are also
358 similar using one approach or another.

359 Domain-average changes of precipitation percentiles are summarized in Table 1 along with
360 separate changes over land and ocean. These changes were computed using the mean of
361 percentiles each region (domain, land, and ocean) for both present and future runs, and then the
362 relative changes with respect to present climate were calculated. PA suggests a decrease in all
363 selected percentiles when aggregating over the entire domain and ocean grid points. It also
364 suggests an increase in all but the 95^{th} percentile over land. EX projects a similar behavior, except
365 for the highest one (99.9^{th}), which increases both over land and ocean. On average, EX produces
366 larger decreases for the 95^{th} and 98^{th} percentiles compared to PA. This difference is strongly
367 dominated by decreases over water in EX, since changes over land are very similar between the
368 two experiments. As we move to more intense precipitation events (99^{th}), the contrast between
369 land and ocean is further enhanced, especially for PA, which suggests substantial changes both
370 over land and ocean but with opposite signs (9.6% vs. -32.6% respectively). Indeed, some large
371 islands such as New Guinea show a strong and statistically significant response of the upper tail
372 to warming in the PA experiment (Fig. 3i).

373 The highest end of the distribution (99.9^{th} percentile) represents events above 10 mm hr^{-1} in
374 most cases and well above 25 mm hr^{-1} in many land grid points (Supplementary Figure S3). In EX,
375 the 99.9^{th} increases over land (14.9%) under climate change conditions, but there is no clear signal
376 over the ocean. In fact, significant changes are mostly located over land. PA shows an increase in
377 extreme precipitation (99.9^{th}) over land (22.4%) too, but it produces significant decreases over the
378 ocean (-10.9%). As a result, PA exhibits a domain-average decrease of high-end extremes (-3.2%),
379 while EX produces an increase (4.0%).

Figure 3 provides a more detailed and visual description of the precipitation response to warming. As opposed to the summary discussed above (Table 1), Figure 3 includes aggregated information on other percentiles (50^{th} to 100^{th}) and shows the spatial variability of changes. Rates below the 90^{th} percentiles are usually light rainfall events (<0.1 mm hr-1) in EX (Supplementary Figure S3), and their contribution to total precipitation is limited. The contribution of events below the 90^{th} percentile to total precipitation may be larger in PA, because the 0.1 mm hr^{-1} rate is reached at a much lower percentile (70^{th}). This is likely due to the drizzle effect that typically affect models with convective schemes [*Gutowski et al.*, 2003; *Sun et al*., 2006; *Dai,* 2006; *Stephens et al.,* 2010; *Pendergrass and Hartmann*, 2014].

Moderate rainfall events (95^{th} percentile) decrease with warming in most locations according to both experiments (Fig. 3c-d). Very few grid-points show an increase of moderate precipitation and they are mostly located over or near the islands. The land-sea contrast becomes increasingly clear in the upper percentiles for both experiments (Fig. 3c-j). However, EX already concentrates rainfall over land much more than PA under present climate conditions, thus the contrast will become even sharper in EX under warming. Therefore, the spatial pattern of mean precipitation changes (Fig. 2) is largely explained by changes in the high-end of the distribution, according to Figure 3.

Overall, explicit and parameterized convection produce different precipitation distributions and different precipitation changes under the same large-scale climate change signal, especially in the upper tail of the distribution. Although the spatial pattern of changes is broadly similar (land-sea contrast), their fine spatial detail, their magnitude, and the response of each percentile to climate change is different between the two convective representations.

3.2 Thermodynamical and dynamical contributions to precipitation changes.

Our experiments suggest that the islands of the Maritime Continent will undergo higher precipitation rates and more intense rainfall extremes in a warmer climate. Mechanisms that produce rainfall changes are often interlaced and their contributions may act in opposite directions. We quantified their combined effect by calculating changes in high percentiles of precipitation and express them as a ratio with respect to the domain-average near-surface warming (*Direct* method). Using near-surface temperature to estimate rainfall scaling imposes important limitations because it does not consider changes in moisture availability, which often play a primary role in defining precipitation extremes [*Lenderink et al.*, 2017]. Also, it assumes homogeneous warming in the vertical and thus does not allow for different changes in the atmospheric water-holding capacity at different vertical levels. However, it is a standard way of measuring the precipitation scaling [*Westra et al.,* 2014; *Bao et al.,* 2017; *Lenderink et al.,* 2017; *Dobrinski et al.,* 2019; *Allan et al.,* 2020] because it relies on widely available observations and model outputs. We also estimated the aggregated contribution of the thermodynamical and dynamical terms of rainfall scaling with temperature using the theoretical approach described in section 2.3 [*O'Gorman and Schneider*, 2009a], and we refer to this method as *Full* scaling. The precipitation scaling was decomposed into thermodynamical and dynamical terms following *Pfahl et al.* [2017]. The *direct* method serves as a backdrop to test the adequacy of the theoretical approach (*full* scaling).

We focus on the scaling of the 99th percentile. For all methods we quantified the scaling by calculating the mean of all events above the percentile for each period and each grid-point, and compute the change relative to present climate values, as we have done with other precipitation changes. Then, we divide it by the domain-average near-surface temperature change and estimate the scaling of intense rainfall with temperature for both experiments (Fig. 4 a-d). The *direct* scaling

425 calculation shows a strong land-sea contrast of the scaling in PA. Most islands undergo increases
426 in the range 10-20% K^{-1}, while much of the ocean experience decreases, sometimes as large as -
427 20% K^{-1}. The spatial pattern of scaling is similar in EX, but the rates are not as pronounced.

428 The *full* scaling estimates (Fig. 4 c-d) yields results that compare very well with the *direct*
429 scaling calculation, including both the pattern and the magnitude of changes. Figure 4 a-d supports
430 the idea that warming leads to processes favoring more intense precipitation over land, while
431 changes of any sign are plausible over water. Ignoring changes in vertical velocities in Eq. 1 (see
432 details in section 2.3), we can estimate the separate contribution of thermodynamic (*Thermo*)
433 processes to the scaling (Fig. 4 e-f). The thermodynamic contribution to extreme precipitation
434 changes is spatially much more homogeneous than the *full* scaling, although it still presents some
435 land-sea contrast in EX. In both experiments, the thermodynamic processes contribute to increases
436 in the range 4.2-8.2% K^{-1} over virtually the entire domain (95% of grid-points), with slightly higher
437 values for EX (4.3-8.2% K^{-1}) than for PA (4.2-7.5% K^{-1}). This is roughly consistent with the
438 Clausius-Clapeyron relationship, which establishes an approximate increase in rainfall rates of 7%
439 per degree of near-surface warming [*Trenberth et al.,* 2003]. The scaling methods produce similar
440 results when using different percentiles (95^{th} and 99.9^{th}, see Supplementary Figures S5 and S6,
441 respectively).

442 In the results above, the vertical pressure velocity (ω_e) was smoothed using a 20-km gaussian
443 filter prior to calculating the scaling. We have also calculated the scaling without the smoothing
444 to determine the impact of this choice (Supplementary Figure S7) and found that the smoothing
445 considerably reduces the noise in both model configurations, particularly in EX. While the overall
446 pattern is similar between the two approaches, the spatial details and magnitude of the *full*
447 (theoretical) scaling is closer to the *direct* scaling when smoothing ω_e.

448 Large spatial variations in *direct* and *full* scaling estimates can only be explained by dynamic
449 processes, because the *thermo* term is spatially homogeneous. The contribution of dynamic
450 processes is calculated as the difference between the *full* scaling and the *thermo* term [*Pfahl et al.*,
451 2017]. The dynamical term enhances or opposes the effect of the thermodynamic mechanisms
452 through changes in vertical motions during extreme precipitation events. Therefore,
453 heterogeneities in vertical motions are responsible for the spatial noise in the dynamical term
454 (Supplementary Figure S8), which modulates the homogeneous thermodynamic contribution. This
455 explains the existence of positive and negative values of *direct* and *full* scaling close together.
456 Although this may be alleviated with longer runs and strengthening the gaussian spatial filter
457 applied to the vertical velocity, differences between the two experiments suggest that the nature of
458 the convective scheme may also play a role in smoothing out spatial heterogeneities of vertical
459 motions. In fact, explicit convection experiments running at few-kilometer resolutions are prone
460 to generate single-grid-cell precipitating systems [*Murata et al.,* 2017a] that may reflect into this
461 spatial noise.
462 In general, our results indicate that the dynamic term counteracts the thermodynamic effect over
463 the ocean. Over land, dynamical processes tend to enhance precipitation scaling in PA. In EX, the
464 dynamic contribution also presents a land-sea contrast, but both positive and negative contributions
465 were obtained over land. This land-sea contrast is consistent with results in *Pfahl et al.* [2017]
466 using GCMs, which suggested that dynamic processes enhanced changes in daily precipitation
467 extremes over large islands in the Maritime Continent. Differences between our two model
468 configurations are further discussed in the next section, where the vertical structure of the
469 atmosphere is analyzed.

3.3 Land-sea thermal contrasts, stability, and precipitation changes.

Our hypothesis is that warming contrasts play a key role in the spatial pattern of the archipelago's rainfall response to a changing climate. Changes in moisture availability due to increased atmospheric water-holding capacity and changes in the large-scale dynamics are spatially too uniform to explain the fine spatial structure of precipitation changes. In the horizontal, land warms faster than the ocean due to their different heat capacity, which intensifies current land-sea thermal contrasts. In the vertical, changes in temperature and humidity profiles may be different at each location, which affects atmospheric stability at different rates. These spatial contrasts create more favorable conditions for mesoscale circulations and increased potential for convective initiation. Whether this potential is realized depends on the convective representation.

For example, future climate change increases the land-sea thermal contrast (Fig. 5a-b) and the domain-average increase is very similar in both experiments. Air over land warms faster (3.30°C in both cases) than the air above the ocean (2.90°C in EX; 2.94°C in PA). Changes in thermal contrast help explain precipitation changes to some extent, as we described in the previous section, but differences between parameterized and explicit runs indicate that the convective representation is crucial to define the rainfall response to this thermal forcing.

Here, we investigate the mechanism that links changes in thermal land-sea contrast and rainfall. The primary source of convective potential over the islands is the moisture flux convergence at the lower levels. Moisture flux convergence was calculated using:

$$MFC = -\nabla \cdot (q\boldsymbol{V}_h) \qquad \text{Eq. 4}$$

Where MFC is the moisture flux convergence, q is water vapor mixing ratio at 2m and $\mathbf{V}_h$ is the horizontal wind vector at 10 m. The approach described by *Bluestein* [1992] was applied to deal with discrete variables.

Because of the enhanced land-sea thermal contrast, the model produces an increase in near-surface MFC along the coastlines (Fig. 5 c-d). This agrees with results in *Tangang et al*. [2020], which also found an increase in low-level moisture flux convergence over the islands using multiple regional climate simulations. This MFC increase on the coastline is accompanied by a decrease far outside over the ocean, where negative values are observed almost everywhere. MFC was decomposed into two terms (horizontal advection of specific humidity and horizontal mass convergence; Eq. 5) following *Banacos and Schultz* [2005]:

$$MFC = -\boldsymbol{V}_h \cdot \nabla q - q\nabla \cdot \boldsymbol{V}_h \qquad \text{Eq. 5}$$

and then changes were calculated for each of them to estimate their relative contribution to MFC changes. This decomposition reveals that MFC changes where largely driven by horizontal convergence changes, while advection changes play a negligible role on average (Fig. 5 e-h).

Therefore, a higher MFC –along the coast and mostly driven by convergence changes– points in the same direction as our hypothesis that mesoscale circulations (sea breeze type) intensify under warmer conditions. This effect is even more marked during the time of the day when sea-breeze usually builds up in the region (10-16 LST, Supplementary Figure S9). Hence, our results are coherent with the idea that land-sea thermal contrasts and the resulting MFC changes are drivers of rainfall redistribution and more intense precipitation over land.

This mechanism may be partly responsible for the intensification of rainfall over land, but there must be other factors (e.g., stability) causing differences in precipitation changes between the two experiments despite their very similar changes in thermal contrasts and MFC.

Under global warming, the upper troposphere warms faster than the lower troposphere in the tropics, which increases dry static stability [*Schneider et al.,* 2010; *Chou et al.,* 2013]. We estimated dry static stability in the lower troposphere from both our experiments using the

514 difference in potential temperature (θ) between the lower (850 hPa) and the middle (500 hPa)
515 troposphere. In both simulations, this difference is reduced in the future, thus indicating increased
516 dry static stability under climate change, especially for the explicit convection run (Supplementary
517 Figure S10). However, these changes in temperature are also accompanied by changes in humidity,
518 which directly affect moist adiabatic processes that govern deep convection. To incorporate this
519 factor, we analyzed changes in potential stability (also called moist static stability or convective
520 stability). Herein, we speak in terms of instability to make the interpretation of results more
521 intuitive, but it is conceptually the same. We examined the equivalent potential temperature (θ_e)
522 and its vertical profiles, which accounts for changes in both temperature and humidity. The
523 difference in θ_e between 900-800 hPa and 600-400 hPa layers provides a measure of potential
524 instability.

525 This choice is motivated by the fact that atmospheric models (e.g., CMIP5 ensemble,
526 Supplementary Figure S11) often show a discontinuity in the vertical derivative of θ_e, which is
527 likely linked to how convective processes are parameterized. The discontinuity is linked to how
528 the schemes work around the freezing level, their interaction with microphysics schemes and the
529 quasi-equilibrium profile used in certain parameterizations such as the Betts-Miller Janjic, which
530 is used in the parameterized simulations here. Indeed, this behavior is also detected in PA around
531 the 500 hPa level. This reflects on changes of the vertical profiles simply because the discontinuity
532 is shifted upwards. To reduce the dependence of our results on this issue, which we assume is a
533 model artifact, we computed potential instability using the above reference layers.

534 Vertical profiles of equivalent potential temperature (θ_e) reveal that time-mean potential
535 instability will increase everywhere under the prescribed climate change signal according to both
536 experiments (Fig. 6c). This is shown by steeper vertical profiles of θ_e under future climate

conditions with the largest increases in θ_e near the surface (~14-15 K). Changes over land are on average very similar between PA and EX, and both show an intensification of instability in the early afternoon (Fig. 6d). On the other hand, changes over the ocean are slightly larger in PA and are flat throughout the day in both model runs. This spatial distribution of potential instability changes is further illustrated in Figure 6 e-f, which suggest that instability will increase the most over large land masses. These changes were tested for statistical significance using a Mann-Whitney U test at the 99% confidence level and they are significant everywhere in the domain. The land-sea contrast of potential instability changes is more pronounced in EX, mostly because EX produces more moderate changes over water. If we select only days when precipitation exceeds the 99.9th percentile in each grid cell and calculate the changes in potential instability, EX produces much stronger changes than PA during such events (Supplementary Figure S12). Therefore, despite similar time-mean changes in potential stability and mean precipitation changes, EX suggest more intense extreme precipitation in a warming climate accompanied by higher potential instability.

To understand the link between this increase in potential instability and precipitation extremes, we focus on potential instability preceding events above the 99.9th percentile. To that purpose, we selected 0.5° by 0.5° areas in the four largest islands (squares in Fig. 1) and calculated the area-averaged potential instability (θ_e^{850hPa}-θ_e^{500hPa}) over the 12 hours before any grid cell exceeds its 99.9th percentile of hourly precipitation. Figure 7 shows the relationship between the intensity of heavy rainfall events versus the preceding potential instability for present and future simulations, both model configurations and over the four selected representative areas. Retaining only dry hours to calculate convective instability as opposed to all preceding hours was tested with no substantial differences (not shown) and we decided to keep the all-hour approach so that all instability values

were calculated using the same number of preceding hours. Different accumulation periods (6, 18, 24 hours) and area sizes (0.2°, 1.0°) were also tested with very similar results (not shown). Different locations within each island were also examined to ensure our results were robust and the outputs were qualitatively the same (Supplementary Figures S14 and S15).

In all cases, the atmosphere reaches a clearly different state where both potential instability and extreme rainfall intensity are higher under a warmer climate. While potential instability alone is not enough to determine the intensity of extreme events for each of the periods separately, this is not surprising since many other factors are involved in the generation of heavy rainfall events, thus the dispersion of the point clouds. However, it indicates that the model response to climate change in terms of precipitation extremes and potential instability are related to each other.

This relationship also reveals an interesting contrast between model runs. The fully explicit convection is much more dispersed in the rainfall-instability space depicted in Fig. 7. Some of the differences between experiments noted before can be interpreted through this feature. For instance, it shows that the convective parameterization restricts the atmospheric conditions to a given range because it continuously adjusts the vertical profile towards an equilibrium state. The explicit run, on the contrary, is more flexible in this sense, and it allows for higher precipitation rates (Supplementary Figure S14 and S15). In fact, it also produces situations with substantially larger potential instability when the extremes occur (Fig. 7). As a result, the response to climate change in PA is spatially more homogeneous than in EX, which produces a noisier signal because of the higher degrees of freedom explicit convection provides. Precipitation rates above the 99.9^{th} percentile were also compared to other variables such as potential temperature (θ), Convective Available Potential Energy (CAPE) and precipitable water (PW) to illustrate their links in a changing climate (Supplementary Figure S16). In agreement with our previous findings, changes

583 in the intensity of extreme rainfall are related to an increase in dry static stability (θ^{850hPa}-θ^{500hPa})
584 and an increase in latent conditional instability (CAPE). It also shows that this contrast between
585 changes in dry static stability (temperature dependent) and convective stability (temperature and
586 moisture dependent) when extremes occur is mostly due to a higher availability of precipitable
587 water, which significantly increases in the future.

588 Present and future bivariate distributions of rainfall and the various instability metrics (Fig. 7
589 and Supplementary Figures S14-S16) were tested statistically to determine if they are significantly
590 different. All present and future bivariate distributions were statistically different to each other at
591 the 0.01 significance level using a multi-dimensional version of the Kolgomorov-Smirnov (KS)
592 test [*Fassano and Franceschini,* 1987]. A classical 1-D KS test was also applied to present and
593 future precipitation distributions and were found different at the 0.01 significance level too.

594 Increased instability only produces precipitation changes if convective circulation is intensified.
595 Thus, changes in vertical motions must be considered to explain the spatial contrasts of rainfall
596 changes (see section 3.2). Here, we relate changes in vertical pressure velocity (ω_e) that precede
597 precipitation extremes with changes in the extremes themselves (Fig. 8). We binned grid points by
598 changes in extreme rainfall (total accumulated above the 99th percentile). For each bin, we
599 computed the average change in the vertical profile of ω_e over the six hours preceding each extreme
600 event. We chose a six-hour period because vertical motions due to convection start approximately
601 six hours before the peak of the precipitation diurnal cycle in the region [*Argüeso et al.* 2020].

602 On average, the atmospheric environment preceding intense rainfall is characterized by
603 ascending motions almost through the entire troposphere in both experiments and climate periods
604 (Supplementary Figures S17 and S18). Only the bottom and the top levels show small positive
605 values (descending motions). Thus, positive changes ω_e can be generally interpreted as a

606 weakening of ascending vertical motions. Both experiments concentrate stronger vertical motions
607 and rainfall extremes over land, which is consistent with the picture described in section 3.2. The
608 average ω_e preceding rainfall extremes and its changes are spatially more homogeneous in the
609 parameterized case (not shown), which is also consistent with the results above (Fig. 7 and
610 Supplementary Figures S14-S16).

611 Not only rainfall extremes are collocated with more intense upward motions, but also their
612 changes. Areas where rainfall extremes will increase the most coincide with stronger upward
613 motions, particularly above 800hPa (red in Fig.8). Likewise, extreme rainfall decreases are
614 accompanied by weakened ascending winds (blue in Fig. 8). Weakened vertical motions (blue)
615 extend across the zero-change line, hence small increases (<20%) in extreme precipitation occur
616 with decreases in vertical rising motions, especially over land and when convection is explicit (Fig.
617 8f). It is likely that changes in ω_e partly offset the effect of warming, but the latter still dominates
618 in this range. These results are consistent with the decomposition of scaling in dynamical and
619 thermodynamical terms, where vertical motions help explain spatial contrasts in extreme rainfall
620 changes. Similar results were obtained for other percentiles too (95^{th} and 99.9^{th}; not shown).

621 Most ocean areas show a decrease in precipitation extremes (99^{th} percentile; Fig. 3g-h and Fig
622 8c-d) and weakening of vertical motions preceding such intense rainfall events (Fig. 8c-d). On the
623 other hand, upward vertical velocity before extreme events tend to intensify where heavy rainfall
624 increases over the ocean.

625 This aggregated view reveals some similarities and differences between the two convective
626 representations. Both runs expand the range of possible extremes to higher values, especially EX
627 (Supplementary Figures S17-S18). They also tend to increase the land-sea contrast of ω_e under a
628 warmer climate, particularly PA, as shown the intensification of blue areas in Fig 8c and read areas

629 in Fig 8e. As for the differences, PA tends to produce larger changes in vertical motions (Fig. 8),
630 and they are spatially more organized and uniform in the vertical (not shown). In the explicit
631 convection run, most changes of extreme precipitation over land lie around 20% (Fig. 8f, top) and
632 vertical motions are weakened in the lower-to-middle troposphere for this range of precipitation
633 and intensified in the atmosphere above. This feature can be interpreted as a deepening of the
634 convective circulation and expansion of the convective cell upwards. *Argüeso et al.* [2020] also
635 found that EX produces deeper convective circulations than PA under present climate condition,
636 a difference that could be enhanced with warming.

637 Therefore, the importance of land masses in the convective development and their role as
638 rainfall attractor in the two model experiments is different. The concentration of rainfall over land
639 seems to strengthen under future climate conditions as the land-sea thermal contrast intensifies and
640 the potential instability increases, because they favor moisture convergence and convective
641 circulations over the islands. However, the model responds differently to these changes depending
642 on how convection is represented, especially in terms of vertical pressure velocity. The need for
643 triggering factors in the explicit case and the constrains imposed by the deep parameterization
644 scheme may help explain these differences in vertical motions and precipitation intensities.

645 # 4 Conclusions

646 We studied the role of horizontal and vertical warming contrasts on precipitation changes in the
647 Maritime Continent for the late 21st century under a RCP8.5 scenario using a Pseudo-Global
648 Warming approach. We analyzed results from a regional climate model operating at convection-
649 permitting scales with two different representations of deep convection: parameterized and
650 explicit.

We found that the model produces a domain-averaged decrease of rainfall during the Maritime Continent wet season (NDJF) for both convective representations, although there is a marked land-ocean contrast. Both model configurations tend to produce a decrease over the ocean and an increase over land. Even though GCMs do not agree on the sign of rainfall changes for the region, their spatial pattern of changes is consistent with the land-ocean contrast we obtained [*Jourdain et al.,* 2013; *Wang et al.,* 2020]. The ensemble mean of GCMs selected in this study projects a domain-average increase in rainfall and in the vertically integrated water vapor. Thus, the decline of domain-average precipitation suggested by our model experiments cannot be explained by changes in the large-scale water vapor supply (i.e., advection). Instead, it must be explained by processes that transform the available water vapor into precipitation and how they are represented in models.

Our experiments suggest that the islands of the Maritime Continent will undergo more intense mean and extreme precipitation in a warmer climate. However, extremes behave differently under the same large-scale climate change signal depending on how convection is represented. This includes their magnitude, spatial pattern, and the relative changes of the various percentiles. The most prominent difference is that the land-sea contrast of changes is more pronounced in the parameterized runs. The upper percentiles of rainfall undergo larger increases relative to present climate extremes when convection is parameterized. However, explicit convection expands the range of possible future extremes to higher values. This is partly because present climate extremes in EX are already more intense than in PA, but also because the convective scheme constrains the response to warming. Therefore, future generations of climate projections at convection-permitting resolutions may project different outlooks for rainfall extremes to those currently available.

673 We determined the contribution of thermodynamical and dynamical processes to changes in
674 rainfall extremes under a warmer climate. Thermodynamic effects account for changes in
675 precipitation extremes that are consistent with the Clausius-Clapeyron relationship, and their
676 contribution is relatively homogeneous across the domain. Thus, we need to invoke dynamical
677 processes to explain features of extreme rainfall changes, such as their magnitude range (-20% K^{-1}
678 to 20% K^{-1}), their spatial contrasts and the divergences between the two model runs.
679 According to our simulations, the primary driver of changes in the spatial distribution of rainfall
680 is the land-sea thermal contrast and its enhancement under climate change. Land warms faster than
681 the ocean, which favors local sea-breeze type circulations. These circulations increase low-level
682 moisture flux convergence over land and contribute to create conditions for deep convection
683 development over land. They are also responsible for suppressing rainfall generation over the
684 ocean to some extent.
685 Deep convection and heavy rainfall require atmospheric instability to occur. Climate change
686 modifies the vertical profile of the atmosphere and thus alters the overall stability. Although dry
687 static stability increases under future climate conditions because the upper half of the troposphere
688 warms faster, the combined effect of temperature and humidity changes in the vertical makes the
689 atmosphere more unstable in terms of moist static stability. While both model experiments show
690 this response to climate change, the convective scheme constrains potential instability and extreme
691 precipitation values within a narrower range. Under future climate conditions, this means the
692 model with explicit convection allows heavier rainfall events to occur. Yet, changes relative to
693 present climate values are higher in the parameterized case. Also, the convective scheme produces
694 a response to climate change that is spatially more uniform, while explicit convection generates
695 noisier patterns of extreme precipitation changes.

Deep convection entails intense upward vertical motions. Thus, extreme precipitation is linked to high vertical pressure velocity. We found that the model tends to concentrate strong vertical motions and rainfall extremes over land, especially when convection is explicitly resolved. In some land areas, this is enhanced in future climate simulations, which explains departures from the thermodynamic contribution to extreme rainfall changes. Changes in vertical winds also indicate a possible expansion of the convective cell over the islands and a slight weakening of upward motions in the mid troposphere. Even though explicit convection produces more extreme rainfall events over land in the future —due to further concentration of upward motions over large islands and the lack of convective scheme constrains—, the parameterized case suggests stronger changes relative to present climate values. In fact, the model produces stronger changes in vertical motions preceding extreme events with climate change when convection is parameterized. This refers not only to the strengthening of vertical winds over land, but also to their weakening over the ocean. In both model configurations, areas of stronger upward vertical pressure velocity are collocated with positive changes in extreme precipitation, and vice versa. This spatial coincidence, together with the scaling decomposition into thermodynamical and dynamical terms, evidences the role of vertical motions in modulating the intensity of future climate rainfall events.

In summary, we showed that the way convection is represented is crucial in defining the model response to warming, because it defines dynamical processes that shape the future distribution of precipitation and the intensity of extremes.

Acknowledgements

This study was supported by REHIPRE and COASTEPS projects. REHIPRE is funded by the European Union's Horizon 2020 Research and Innovation Programme under the Marie Skłodowska-Curie Actions Individual Fellowship Grant Agreement 743547 (H2020-MSCA-IF-

2016-743547). The COASTEPS project (CGL2017-82868-R MEIC/AEI/EU FEDER) is financed by the Spanish Ministry of Economy, Industry and Competitiveness, and partially funded by the EU FEDER funds. D. Argüeso was also funded by Spanish Ministry of Science and Innovation through the Research Project EPICC project (PID2019-105253RJ-I00) and the Beatriz Galindo Programme (BG20/00078). We thankfully acknowledge the computer resources at MareNostrum 4 and the technical support provided by the Barcelona Supercomputing Center (AECT-2018-3-0002 and AECT-2019-1-0002). We also thank NCAR and other participating institutions for making the WRF-ARW Model publicly available. We acknowledge the World Climate Research Programme's Working Group on Coupled Modelling, which is responsible for CMIP, and we thank each of the climate modelling groups for producing and making available their model output. For CMIP the U.S. Department of Energy's Program for Climate Model Diagnosis and Intercomparison provides coordinating support and led development of software infrastructure in partnership with the Global Organization for Earth System Science Portals. CMIP5 data were obtained from the Australian node of the Earth System Grid Federation (ESGF), hosted at the National Computing Infrastructure (NCI). Furthermore, we acknowledge the ECWMF for providing the ERA5 reanalysis data. As Associate Investigators of the ARC Centre of Excellence for Climate Extremes (Australia), D. Argüeso and A. Di Luca would also like to thank their scientific and technical support. We thank Steve Sherwood for his insights on changes in equivalent potential temperature. We would like to thank two anonymous reviewers whose comments helped improve and clarify this manuscript.

Data availability statement

741 The data on which this paper is based is too large (~ 120TB) to be publicly archived with
742 available resources. The model version used in this study is open source and publicly available
743 (https://github.com/NCAR/WRFV3/releases). Sample namelists to reproduce the experiments are
744 archived and available in a public repository (10.5281/zenodo.4624353). All retained data is
745 available upon request addressed to Daniel Argüeso (d.argueso@uib.es).

746 # References

747 Argüeso, D., A. Di Luca, and J. P. Evans (2016), Precipitation over urban areas in the western
748 Maritime Continent using a convection-permitting model, *Clim. Dyn.*, *47*(3), 1143–1159,
749 doi:10.1007/s00382-015-2893-6.

750 Argüeso, D., R. Romero, and V. Homar (2020), Precipitation Features of the Maritime
751 Continent in Parameterized and Explicit Convection Models, *J. Climate*, *33*(6), 2449–2466,
752 doi:10.1175/JCLI-D-19-0416.1.

753 Banacos, P. C., and D. M. Schultz (2005), The use of moisture flux convergence in forecasting
754 convective initiation: Historical and operational perspectives, *Wea. Forecasting*, *20*(3), 351–366,
755 doi:10.1175/WAF858.1.

756 Baranowski, D. B., D. E. Waliser, X. Jiang, J. A. Ridout, and M. K. Flatau (2019),
757 Contemporary GCM Fidelity in Representing the Diurnal Cycle of Precipitation Over the Maritime
758 Continent, *J. Geophys. Res. Atmos.*, *124*(2), 747–769, doi:10.1029/2018JD029474.

759 Birch, C. E., M. J. Roberts, L. Garcia-Carreras, D. Ackerley, M. J. Reeder, A. P. Lock, and R.
760 Schiemann (2015), Sea-Breeze Dynamics and Convection Initiation: The Influence of Convective
761 Parameterization in Weather and Climate Model Biases, *J. Climate*, *28*(20), 8093–8108,
762 doi:10.1175/JCLI-D-14-00850.1.

763 Birch, C. E., S. Webster, S. C. Peatman, D. J. Parker, A. J. Matthews, Y. Li, and M. E. E.
764 Hassim (2016), Scale Interactions between the MJO and the Western Maritime Continent, *J.*
765 *Climate*, *29*(7), 2471–2492, doi:10.1175/JCLI-D-15-0557.1.
766 Bony, S., G. Bellon, D. Klocke, S. Sherwood, S. Fermepin, and S. Denvil (2013), Robust direct
767 effect of carbon dioxide on tropical circulation and regional precipitation, *Nature Geoscience*, *6*(6),
768 447–451, doi:10.1038/ngeo1799.
769 Cai, W., G. Wang, B. Dewitte, L. Wu, A. Santoso, K. Takahashi, Y. Yang, A. Carréric, and M.
770 J. McPhaden (2018), Increased variability of eastern Pacific El Niño under greenhouse warming,
771 *Nature*, 564(7735), 201–206, doi:10.1038/s41586-018-0776-9.
772 Chan, S. C., E. J. Kendon, N. M. Roberts, H. J. Fowler, and S. Blenkinsop (2016), Downturn
773 in scaling of UK extreme rainfall with temperature for future hottest days. *Nature Geoscience*, 9,
774 24–28, https://doi.org/10.1038/ngeo2596.
775 Chen, J., Z. Wang, C.-Y. Tam, N.-C. Lau, D.-S. D. Lau, and H.-Y. Mok (2020), Impacts of
776 climate change on tropical cyclones and induced storm surges in the pearl River Delta region using
777 pseudo-global- warming method, *Sci. Rep.*, 1–10, doi:10.1038/s41598-020-58824-8.
778 Chou, C., Chiang, J. C. H., Lan, C. W., Chung, C. H., Liao, Y. C., & Lee, C. J. (2013). Increase
779 in the range between wet and dry season precipitation. *Nature Geoscience*, 6(4), 263–267.
780 https://doi.org/10.1038/ngeo1744
781 Contractor, S., M.G. Donat, and L.V. Alexander (2018), Intensification of the Daily Wet Day
782 Rainall Distribution Across Australia, *Geophys. Res. Lett.*, 45, 8568-8576, doi:
783 10.1029/2018GL078875

784 Contractor, S., M.G. Donat, and L.V. Alexander (2021), Changes in Observed Daily
785 Precipitation over Global Land Areas since 1950, *J. Climate*, 34(1), 3-19, doi: 10.1175/JCLI-D-
786 19-0965.1

787 Dai, A. (2006), Precipitation characteristics in eighteen coupled climate models, *J. Climate*,
788 19(18), 4605-4630, doi: 10.1175/JCLI3884.1

789 Donat-Magnin, M., N. C. Jourdain, C. Kittel, C. Agosta, C. Amory, H. Gallée, G. Krinner, and
790 M. Chekki (2021), Future surface mass balance and surface melt in the Amundsen sector of the
791 West Antarctic Ice Sheet, *The Cryosphere*, 15, 571–593, doi:10.5194/tc-15-571-2021.

792 Drobinski, P. et al. (2018), Scaling precipitation extremes with temperature in the
793 Mediterranean: past climate assessment and projection in anthropogenic scenarios, *Clim. Dyn*.,
794 51(3), 1237–1257, doi:10.1007/s00382-016-3083-x.

795 Dutheil, C., M. Lengaigne, M. Bador, J. Vialard, J. Lefèvre, N. Jourdain, S. Jullien, A. Peltier,
796 B. Sultan, and C. Menkès (2020), Impact of projected sea surface temperature biases on tropical
797 cyclones projections in the South Pacific, *Sci. Rep.*, 1–12, doi:10.1038/s41598-020-61570-6.

798 Fasano, G., and A. Franceschini (1987), A multidimensional version of the Kolmogorov-
799 Smirnov test. *Mon. Not. R. Astr. Soc.*, 225, 155-170, doi: 10.1093/mnras/225.1.155.

800 Fiedler, S. et al. (2020), Simulated Tropical Precipitation Assessed across Three Major Phases
801 of the Coupled Model Intercomparison Project (CMIP), *Mon. Wea. Rev.*, *148*(9), 3653–3680,
802 doi:10.1175/MWR-D-19-0404.1.

803 Fosser, G., E. J. Kendon, D. Stephenson, and S. Tucker (2020), Convection- Permitting Models
804 Offer Promise of More Certain Extreme Rainfall Projections, *Geophys. Res. Lett.*, *47*(13), 1–9,
805 doi:10.1029/2020GL088151.

806 Gutowski Jr., W., Decker, S., Donavon, R., Pan, Z., Arritt, R., and Takle, E (2003), Temporal-
807 spatial scales of observed and simulated precipitation in central U.S. climate, *J. Climate*, 16, 3841–
808 3847, doi: 10.1175/1520-0442(2003)016%3C3841:TSOOAS%3E2.0.CO;2
809 Hassim, M. E. E., T. P. Lane, and W. W. Grabowski (2016), The diurnal cycle of rainfall over
810 New Guinea in convection-permitting WRF simulations, *Atmos. Chem. Phys.*, *16*(1), 161–175,
811 doi:10.5194/acp-16-161-2016.
812 Held, I. M., and B. J. Soden (2006), Robust responses of the hydrological cycle to global
813 warming, *J. Climate*, *19*(21), 5686–5699, doi:10.1175/JCLI3990.1.
814 Hersbach, H., Bell, B., Berrisford, P., Hirahara, S., Horányi, A., Muñoz- Sabater, J., and others
815 (2020). The ERA5 global reanalysis. *Q.J.R. Meteorol. Soc*, 146(730), 1999-2049, doi:
816 10.1002/qj.3803.
817 Hong, S. Y., and J. Lim (2006), The WRF single-moment 6-class microphysics scheme
818 (WSM6), *J Korean Meteor Soc*, *42*(2), 129–151.
819 Im, E. S., and E. Elthair (2018), Simulation of the diurnal variation of rainfall over the western
820 Maritime Continent using a regional climate model, *Clim. Dyn.*, *51*(1-2), 73–88,
821 doi:10.1007/s00382-017-3907-3.
822 IPCC, 2013: Annex I: Atlas of Global and Regional Climate Projections Supplementary
823 Material RCP8.5 [van Oldenborgh, G.J., M. Collins, J. Arblaster, J.H. Christensen, J. Marotzke,
824 S.B. Power, M. Rummukainen and T. Zhou (eds.)]. In: Climate Change 2013: The Physical
825 Science Basis. Contribution of Working Group I to the Fifth Assessment Report of the
826 Intergovernmental Panel on Climate Change [Stocker, T.F., D. Qin, G.-K. Plattner, M. Tignor,
827 S.K. Allen, J. Boschung, A. Nauels, Y. Xia, V. Bex and P.M. Midgley (eds.)]. Available from
828 www.climatechange2013.org and www.ipcc.ch.

829 Joshi, M. M., J. M. Gregory, M. J. Webb, D. M. H. Sexton, and T. C. Johns (2007), Mechanisms
830 for the land/sea warming contrast exhibited by simulations of climate change, *Clim. Dyn.*, *30*(5),
831 455–465, doi:10.1007/s00382-007-0306-1.
832 Jourdain, N.C, A. Sen Gupta, A.S. Taschetto, C.C. Ummenhofer, A.F. Moise and K. Ashok
833 (2013), The Indo-Australian monsoon and its relationship to ENSO and IOD in reanalysis data and
834 the CMIP3/CMIP5 simulations, *Clim. Dyn.*, 41, 3073–3102, doi: 10.1007/s00382-013-1676-1.
835 Knutti, R., R. Furrer, C. Tebaldi, J. Cermak, and G. A. Meehl (2010), Challenges in Combining
836 Projections from Multiple Climate Models, *J. Climate*, *23*(10), 2739–2758,
837 doi:10.1175/2009JCLI3361.1.
838 Krinner, G., and M. G. Flanner (2018), Striking stationarity of large-scale climate model bias
839 patterns under strong climate change, *PNAS*, *115*(38), 9462–9466, doi:10.1073/pnas.1807912115.
840 Lambert, F. H., A. J. Ferraro, and R. Chadwick (2017), Land–Ocean Shifts in Tropical
841 Precipitation Linked to Surface Temperature and Humidity Change, *J. Climate*, *30*(12), 4527–
842 4545, doi:10.1175/JCLI-D-16-0649.1.
843 Li, Y., A. Sen Gupta, A. S. Taschetto, N. C. Jourdain, A. Di Luca, J. M. Done, and J.-J. Luo
844 (2020), Assessing the role of the ocean–atmosphere coupling frequency in the western Maritime
845 Continent rainfall, *Clim. Dyn.*, *54*(11), 4935–4952, doi:10.1007/s00382-020-05266-7.
846 Li, Y., N. C. Jourdain, A. S. Taschetto, A. Sen Gupta, D. Argüeso, S. Masson, and W. Cai
847 (2016), Resolution dependence of the simulated precipitation and diurnal cycle over the Maritime
848 Continent, *Clim. Dyn.*, *48*(11-12), 1–20, doi:10.1007/s00382-016-3317-y.
849 Ling, J., C. Zhang, R. Joyce, P. P. Xie, and G. Chen (2019), Possible Role of the Diurnal Cycle
850 in Land Convection in the Barrier Effect on the MJO by the Maritime Continent, *Geophys. Res.*
851 *Lett.*, *46*(5), 3001–3011, doi:10.1029/2019GL081962.

852 Lucas-Picher, P., D. Argüeso, E. Brisson, Y. Tremblay, P. Berg, A. Lemonsu, S. Kotlarski and
853 C. Caillaud (2021) Convection-permitting modelling with regional climate models: latest
854 developments and next steps. WIREs Climate Change, 12(6): e731, doi: 10.1002/wcc.731
855 Narsey, S. Y., J. R. Brown, R. A. Colman, F. Delage, S. B. Power, A. F. Moise, and H. Zhang
856 (2020), Climate Change Projections for the Australian Monsoon from CMIP6 Models, *Geophys.*
857 *Res. Lett.*, *47*(13), 147–9, doi:10.1029/2019GL086816.
858 Neale, R., and J. Slingo (2003), The maritime continent and its role in the global climate: A
859 GCM study, *J. Climate*, *16*(5), 834–848, doi:10.1175/1520-
860 0442(2003)016<0834:TMCAIR>2.0.CO;2.
861 O'Gorman, P. A., and T. Schneider (2009a), Scaling of Precipitation Extremes over a Wide
862 Range of Climates Simulated with an Idealized GCM, *J. Climate*, *22*(21), 5676–5685,
863 doi:10.1175/2009JCLI2701.1.
864 O'Gorman, P. A., and T. Schneider (2009b), The physical basis for increases in precipitation
865 extremes in simulations of 21st-century climate change, *PNAS*, *106*(35), 14773–14777,
866 doi:10.1073/pnas.0907610106.
867 Peatman, S. C., A. J. Matthews, and D. P. Stevens (2014), Propagation of the Madden-Julian
868 Oscillation through the Maritime Continent and scale interaction with the diurnal cycle of
869 precipitation, *Q.J.R. Meteorol. Soc.*, *140*(680), 814–825, doi:10.1002/qj.2161.
870 Pendergrass, A.G., and D.L. Hartmann (2014), Two modes of change of the distribution of rain,
871 *J. Climate*, 27(22), 8357-8371, doi: 10.1175/JCLI-D-14-00182.1.
872 Pfahl, S., P. A. O'Gorman, and E. M. Fischer (2017), Understanding the regional pattern of
873 projected future changes in extreme precipitation, *Nat Clim Change*, *7*(6), 423–427,
874 doi:10.1038/nclimate3287.

875 Prein, A. F. et al. (2015), A review on regional convection-permitting climate modeling:
876 Demonstrations, prospects, and challenges, *Rev Geophys*, *53*(2), 323–361,
877 doi:10.1002/2014RG000475.
878 Prein, A. F., R. Rasmussen, C. L. Castro, A. Dai, and J. Minder (2020), Special issue: Advances
879 in convection-permitting climate modeling, *Clim. Dyn.*, *55*(1), 1–2, doi:10.1007/s00382-020-
880 05240-3.
881 Qian, J.-H. (2008), Why Precipitation Is Mostly Concentrated over Islands in the Maritime
882 Continent, *J. Atmos. Sci.*, *65*(4), 1428–1441, doi:10.1175/2007JAS2422.1.
883 Qian, J.-H., A. W. Robertson, and V. Moron (2010), Interactions among ENSO, the Monsoon,
884 and Diurnal Cycle in Rainfall Variability over Java, Indonesia, *J. Atmos. Sci.*, *67*(11), 3509–3524,
885 doi:10.1175/2010JAS3348.1.
886 Ruppert, J. H., and F. Zhang (2019), Diurnal forcing and phase locking of gravity waves in the
887 maritime continent, *J. Atmos. Sci.*, *76*(9), 2815–2835, doi:10.1175/JAS-D-19-0061.1.
888 Ruppert, J. H., Jr., and X. Chen (2020), Island Rainfall Enhancement in the Maritime Continent,
889 *Geophys. Res. Lett.*, *47*(5), 1–9, doi:10.1029/2019GL086545.
890 Schär, C., C. Frei, D. Lüthi, and H. C. Davies (1996), Surrogate climate-change scenarios for
891 regional climate models, *Geophys. Res. Lett.*, *23*(6), 669–672, doi:10.1029/96GL00265.
892 Schär, C. et al. (2016), Percentile indices for assessing changes in heavy precipitation events,
893 *Climatic Change*, *137*(1-2), 201–216, doi:10.1007/s10584-016-1669-2.
894 Schiemann, R., M. E. Demory, M. S. Mizielinski, M. J. Roberts, L. C. Shaffrey, J. Strachan,
895 and P. L. Vidale (2013), The sensitivity of the tropical circulation and Maritime Continent
896 precipitation to climate model resolution, *Clim. Dyn.*, *42*(9-10), 2455–2468, doi:10.1007/s00382-
897 013-1997-0.

898 Schneider, T., P. A. O'Gorman, and X. Levine (2010), Water vapor and the dynamics of climate
899 changes, *Rev. Geophys*., 48, RG3001. doi:10.1029/2009RG000302.
900 Seneviratne, S. I., X. Zhang, M. Adnan, W. Badi, C. Dereczynski, A. Di Luca, S. Ghosh, I.
901 Iskandar, J. Kossin, S. Lewis, F. Otto, I. Pinto, M. Satoh, S. M. Vicente-Serrano, M. Wehner, B.
902 Zhou, 2021, Weather and Climate Extreme Events in a Changing Climate. In: Climate Change
903 2021: The Physical Science Basis. Contribution of Working Group I to the Sixth Assessment
904 Report of the Intergovernmental Panel on Climate Change [Masson-Delmotte, V., P. Zhai, A.
905 Pirani, S. L. Connors, C. Péan, S. Berger, N. Caud, Y. Chen, L. Goldfarb, M. I. Gomis, M. Huang,
906 K. Leitzell, E. Lonnoy, J. B. R. Matthews, T. K. Maycock, T. Waterfield, O. Yelekçi, R. Yu and
907 B. Zhou (eds.)]. Cambridge University Press. In Press.
908 Seth, A., A. Giannini, M. Rojas, S.A. Rauscher, S. Bordoni, D. Singh, and S.J. Camargo (2019)
909 Monsoon Responses to Climate Changes—Connecting Past, Present and Future. *Curr. Clim.*
910 *Change Rep.,* 5, 63–79. doi:10.1007/s40641-019-00125-y
911 Skamarock, W. C., J. B. Klemp, J. Dudhia, D. O. Gill, D. M. barker, M. G. Duda, X.-Y. Huang,
912 W. Wang, and J. G. Powers (2008), A Description of the Advanced Research WRF Version 3,
913 *NCAR/TN-475+STR NCAR TECHNICAL NOTE*, 125.
914 Stephens, G. L., T. L'Ecuyer, R. Forbes, A. Gettlemen, J.- C. Golaz, A. Bodas- Salcedo, K.
915 Suzuki, P. Gabriel, and J. Haynes (2010), Dreary state of precipitation in global models, *J.*
916 *Geophys. Res.*, 115, D24211, doi:10.1029/2010JD014532.
917 Sun, Y., Solomon, S., Dai, A., & Portmann, R. W. (2006). How often does it rain? *J. Climate*,
918 19, 916–934. https://doi.org/10.1175/ JCLI3672.1.1996

Supari et al. (2020), Multi-model projections of precipitation extremes in Southeast Asia based on CORDEX-Southeast Asia simulations, *Environmental Research*, *184*, 109350, doi:10.1016/j.envres.2020.109350.

Tangang, F. et al. (2020), Projected future changes in rainfall in Southeast Asia based on CORDEX–SEA multi-model simulations, *Clim. Dyn.*, *55*(5), 1247–1267, doi:10.1007/s00382-020-05322-2.

Trenberth, K. E. (1999), Conceptual framework for changes of extremes of the hydrological cycle with climate change, *Climatic Change*, *42*(1), 327–339, doi:10.1023/A:1005488920935.

Trenberth, K. E., A. Dai, R.M. Rasmussen, and D.B. Parsons, The changing character of precipitation, *Bull. Am. Meteorol. Soc.* 84, 1205-1217, doi: 10.1175/BAMS-84-9-1205.

Vincent, C. L., and T. P. Lane (2017), A 10-Year Austral Summer Climatology of Observed and Modeled Intraseasonal, Mesoscale, and Diurnal Variations over the Maritime Continent, *J. Climate*, *30*(10), 3807–3828, doi:10.1175/JCLI-D-16-0688.1.

Vincent, C. L., and T. P. Lane (2018), Mesoscale Variation in Diabatic Heating around Sumatra, and Its Modulation with the Madden–Julian Oscillation, *Mon. Wea. Rev.*, *146*(8), 2599–2614, doi:10.1175/MWR-D-17-0392.1.

Wang, B., C. Jin, and J. Liu (2020), Understanding Future Change of Global Monsoons Projected by CMIP6 Models, *J. Climate*, *33*(15), 6471–6489, doi:10.1175/JCLI-D-19-0993.1.

Wei, Y., Z. Pu, and C. Zhang (2020), Diurnal Cycle of Precipitation Over the Maritime Continent Under Modulation of MJO: Perspectives from Cloud- Permitting Scale Simulations, *J. Geophys. Res. Atmos.*, *125*(13), 2019–28, doi:10.1029/2020JD032529.

940 Yamanaka, M. D., S.-Y. Ogino, P.-M. Wu, H. Jun-Ichi, S. Mori, J. Matsumoto, and F.
941 Syamsudin (2018), Maritime continent coastlines controlling Earth's climate, *Prog Earth Planet*
942 *Sci*, *5*(1), 1–28, doi:10.1186/s40645-018-0174-9.
943 Yang, S., T. Zhang, Z. Li, and S. Dong (2020), Climate Variability over the Maritime Continent
944 and Its Role in Global Climate Variation: A Review, *J Meteorol Res*, *33*(6), 993–1015,
945 doi:10.1007/s13351-019-9025-x.
946 Yim, B. Y., S.-W. Yeh, H.-J. Song, D. Dommenget, and B. J. Sohn (2017), Land-sea thermal
947 contrast determines the trend of Walker circulation simulated in atmospheric general circulation
948 models, *Geophys. Res. Lett.*, *44*(11), 5854–5862, doi:10.1002/2017GL073778.
949 Yoshikane, T., F. Kimura, H. Kawase, and T. Nozawa (2012), Verification of the Performance
950 of the Pseudo-Global-Warming Method for Future Climate Changes during June in East Asia,
951 *SOLA*, *8*(0), 133–136, doi:10.2151/sola.2012-033.
952
953
954
955
956
957
958
959
960
961

962 **Table 1:** Domain-average changes in mean precipitation and the upper percentiles of hourly
963 rainfall for the parameterized (PA) and explicit (EX) convection experiments. Changes for all
964 grid points, land-only grid points and ocean-only grid points. Changes are in percentage with
965 respect to present climate and positive changes are in bold typeface.

		Mean	95^{th}	98^{th}	99^{th}	99.9^{th}
PA	Total	-13.3	-9.8	-14.4	-19.2	-3.2
	Ocean	-20.2	-11.8	-22.0	-32.6	-10.9
	Land	**4.3**	-5.3	**1.5**	**9.6**	**22.4**
EX	Total	-6.2	-18.9	-17.3	-12.8	**4.0**
	Ocean	-12.7	-47.1	-33.4	-23.7	**0.6**
	Land	**5.0**	-5.3	**0.6**	**5.4**	**14.9**

966

967

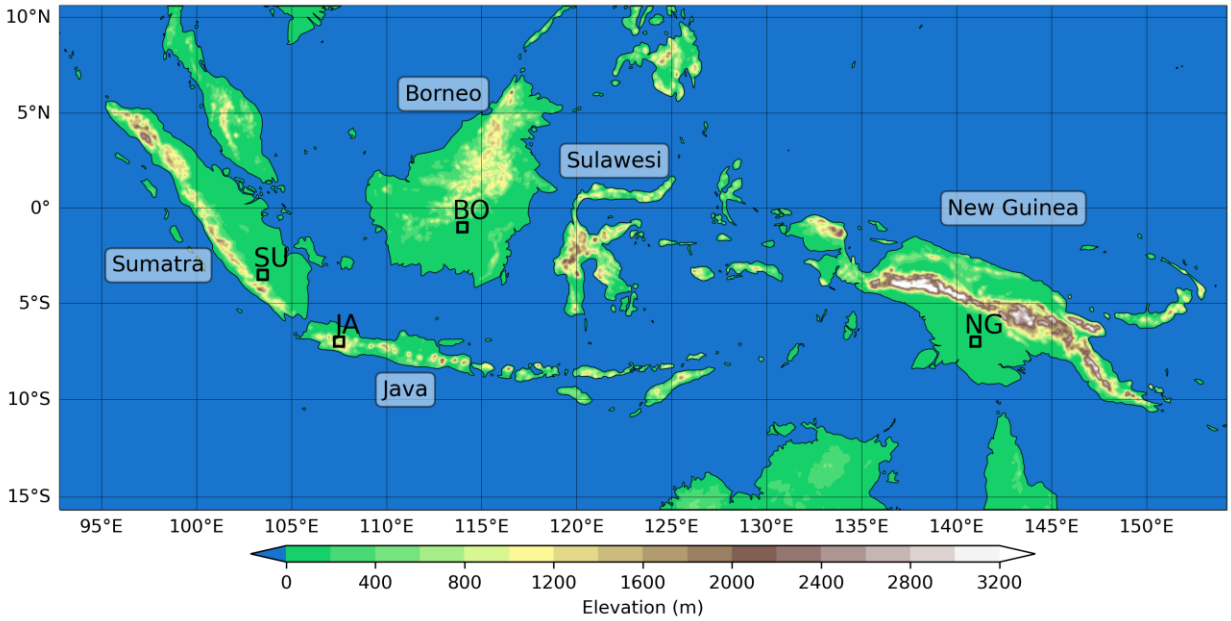

968

969 **Figure 1:** The Maritime Continent archipelago. The region shown corresponds to the model

970 domain and the black squares are sampling areas.

971

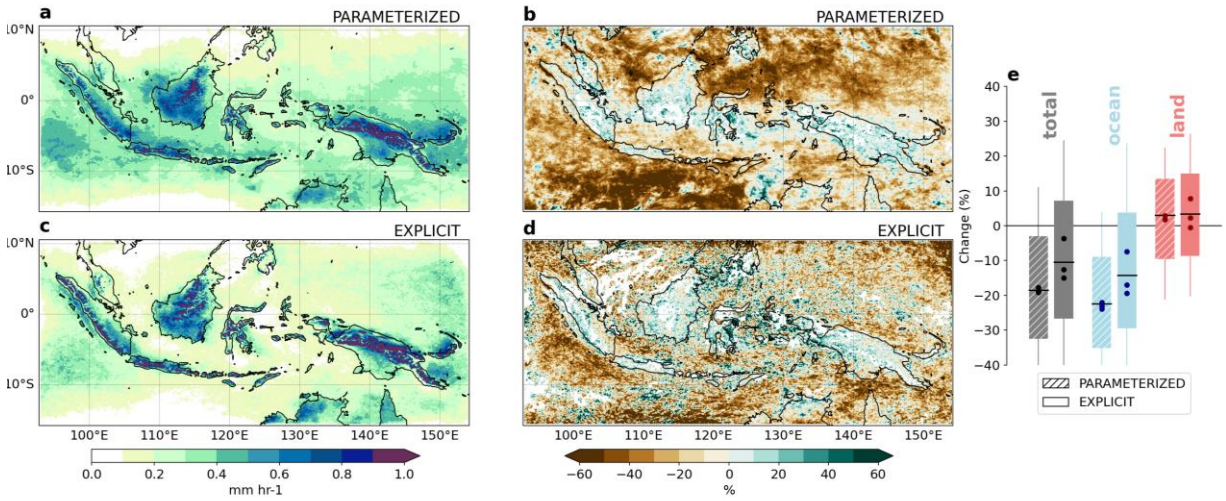

972

973 **Figure 2:** Present mean precipitation rates in the parameterized (a) and the explicit convection

974 runs (c). Relative mean precipitation changes using PGW approach (future minus present) for

975 parameterized (b) and explicit (d) convection runs. Areas with no statistically significant changes

according to a Mann-Whitney U test at the 99% confidence level are masked out in (b) and (d). These areas are 7.9% and 14.7% of the domain, respectively. Boxplots show changes for all (gray), ocean-only (blue) and land-only (red) grid cells for parameterized (hatched) and explicit (solid) experiments. The boxes represent the interquartile range, whiskers are the 10^{th}-90^{th} percentile range, horizontal lines are the median changes over all grid points in each category, and markers show the median for each of the 4-month periods individually.

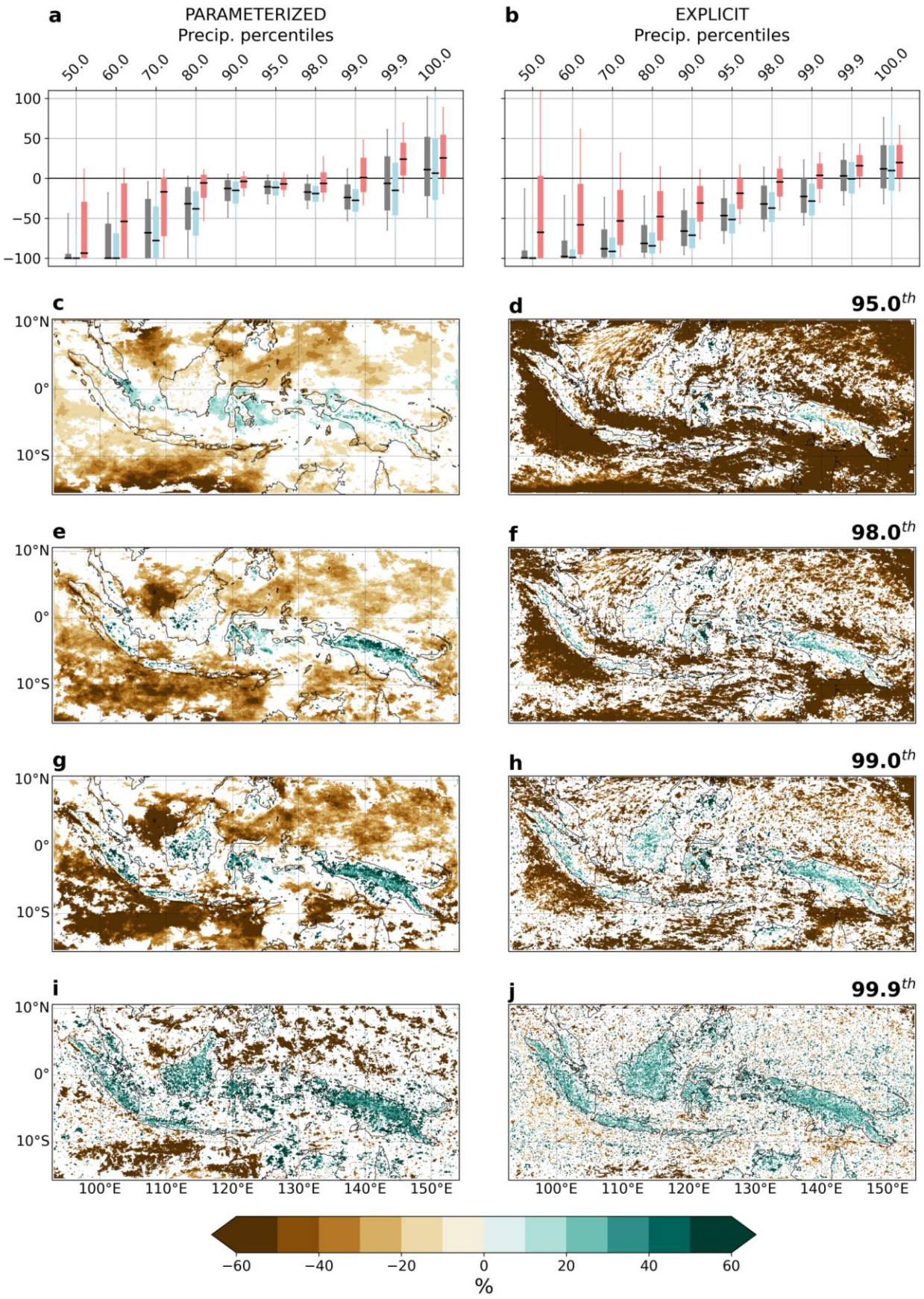
a
PARAMETERIZED
Precip. percentiles
b
EXPLICIT
Precip. percentiles
50.0
60.0
70.0
80.0
90.0
95.0
98.0
99.0
99.9
100.0
100
50
0
−50
−100
c
d
95.0th
e
f
98.0th
g
h
99.0th
i
j
99.9th
10°N
0°
10°S
100°E
110°E
120°E
130°E
140°E
150°E
−60
−40
−20
0
20
40
60
%

983

Figure 3: Changes in rainfall percentiles. Statistics of changes over the entire domain (gray), ocean-only (blue) and land-only (red) grid points for the parameterized (a) and the explicit case (b). Boxes represent the interquartile range; whiskers are the 10^{th}-90^{th} percentile range and horizontal lines are the medians. Spatial patterns of relative changes in rainfall for the 95^{th} (c, d), 98^{th} (e, f), 99^{th} (g, h) and 99.9^{th} (i, j) percentiles for the parameterized (left column) and explicit (right column) model setups. Statistical significance was tested using a bootstrap approach based on 12-hour blocks resampling with replacement repeated 1000 times. According to the test, 43.2%, 46.7%, 42.1% and 19.5% of all the grid-points show significant changes for the corresponding percentiles in the parameterized runs, and 52,2%, 35.3%, 25.8% and 13.1% for the explicit case. Non-significant changes were masked out.

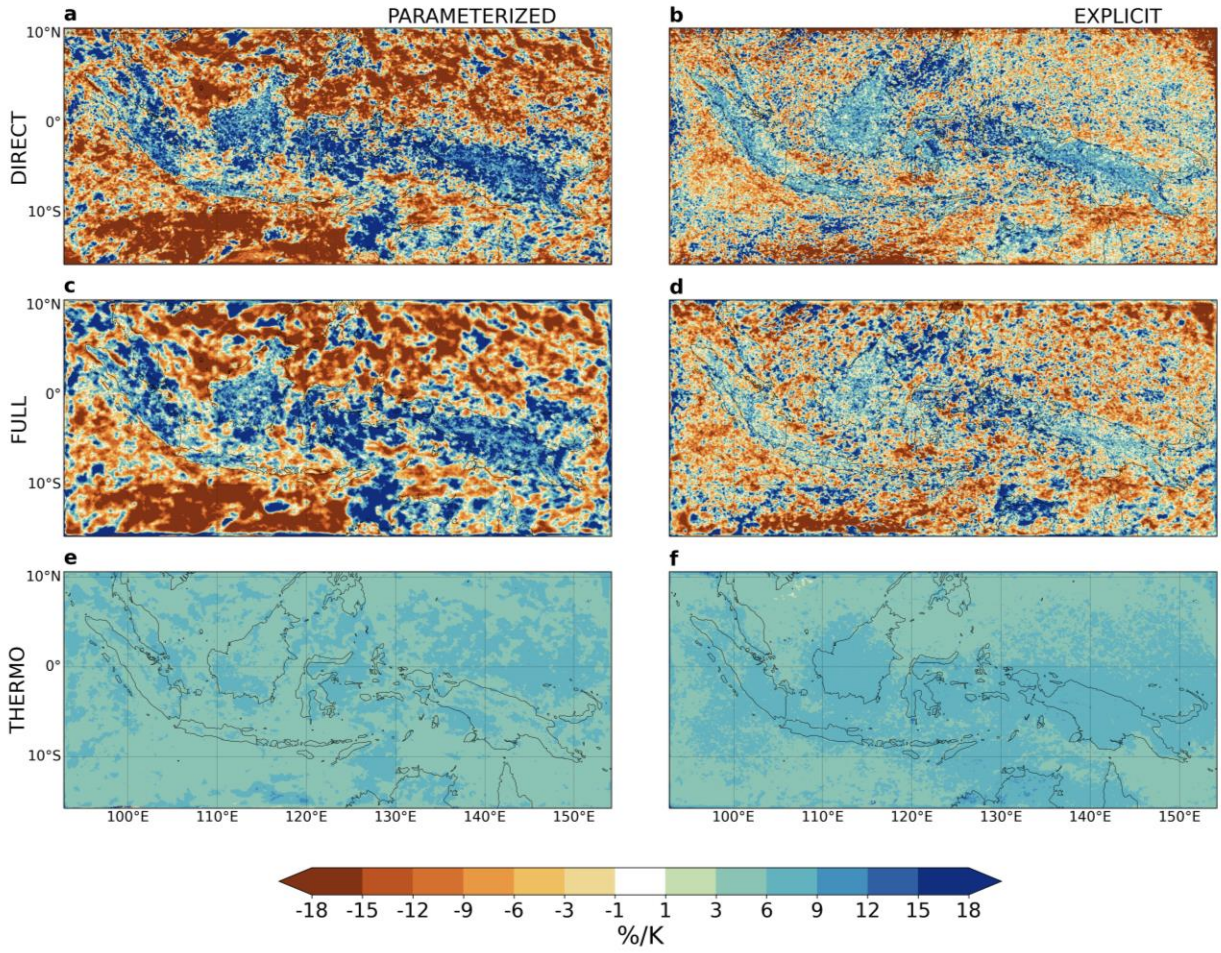

995

996 **Figure 4:** Scaling of the 99th percentile of precipitation with respect to the domain-average 2-m
997 temperature change using hourly precipitation outputs from the model (*direct* scaling; a, b), the
998 full scaling as estimated by the theoretical diagnostic from O'Gorman and Schenider [2009b] (c,
999 d) and the thermodynamic scaling as approximated by Pfahl et al. [2017] (e, f). Left column is for
1000 the parameterized experiment and right column is for the explicit simulation.

1001

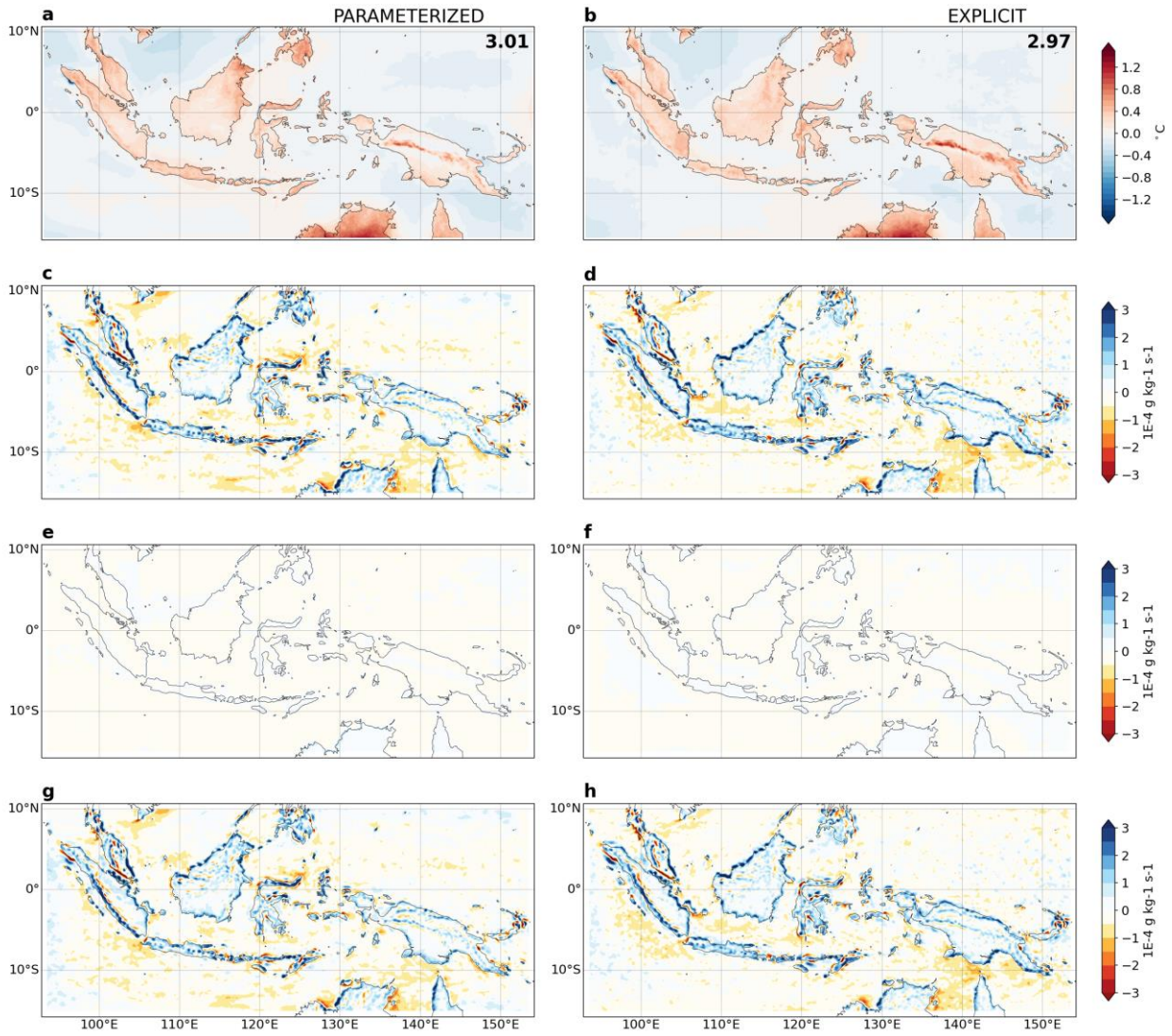

Figure 5: Near-surface temperature (2 m) changes with respect to the domain average warming (top-left numbers in panels a and b) over the entire period (NDJF 2013-2016) for parameterized (a) and fully explicit (b) convection runs. Changes in near-surface moisture flux convergence (spatially smoothed using a gaussian filter with standard deviation of 3 grid points) for parameterized (c) and fully explicit (d) experiments. Changes in MFC due to advection changes (e, f) and convergence changes (g, h) following decomposition in *Banacos and Schulzt* [2005].

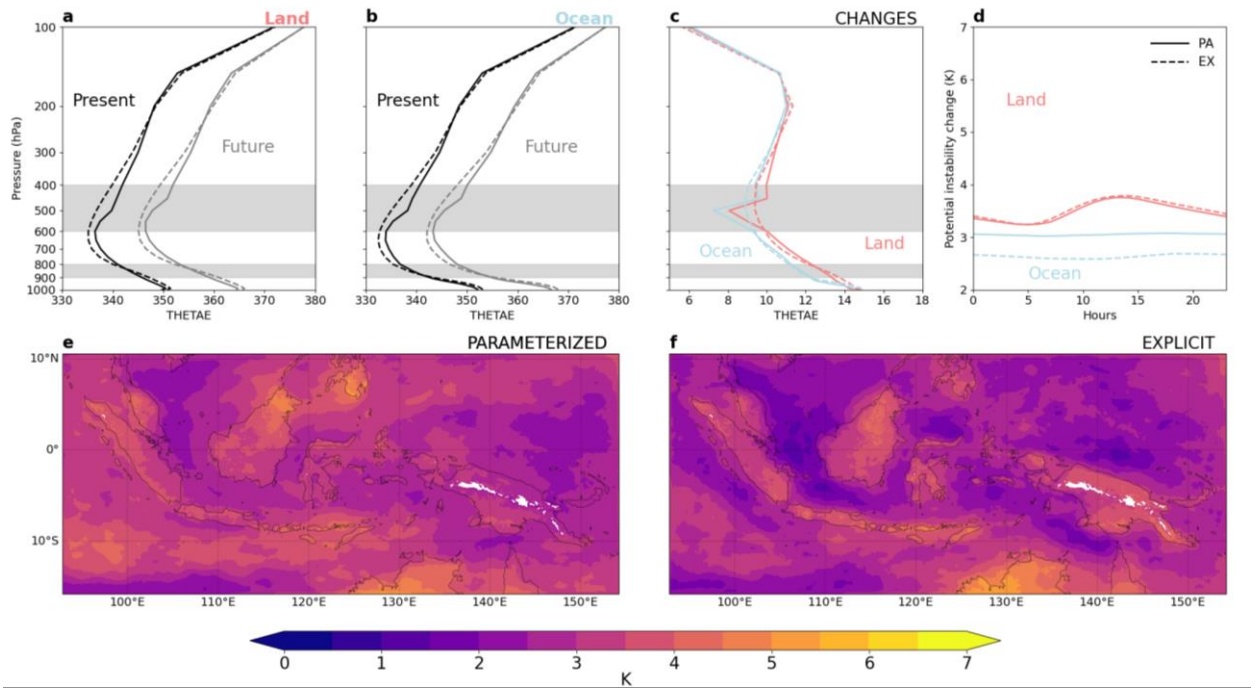

1011

1012 **Figure 6:** Atmospheric potential instability changes in parameterized and explicit convection runs.
1013 Time-averaged mean vertical profiles of θ_e over land grid points (a) and ocean grid points (b) and
1014 their changes (future minus present) (c). Black is for present climate and gray for future climate.
1015 Blue lines are changes over water only and red lines are changes over land only. Solid lines show
1016 parameterized convection experiments and dashed lines are for explicit convection runs. Diurnal
1017 cycle (d) of potential instability changes (θ_e^{850hPa}- $\theta_e^{500\text{hPa}}$) for ocean (blue) and land (red) grid-
1018 points, and parameterized (solid) and explicit (dashed) convection experiments. Spatial
1019 distribution of potential instability changes for the parameterized (e) and explicit (f) convection
1020 simulations. Changes were statistically significant at the 99% confidence level in all grid points
1021 according to a two-sided Mann-Whitney U test.

1022

1023

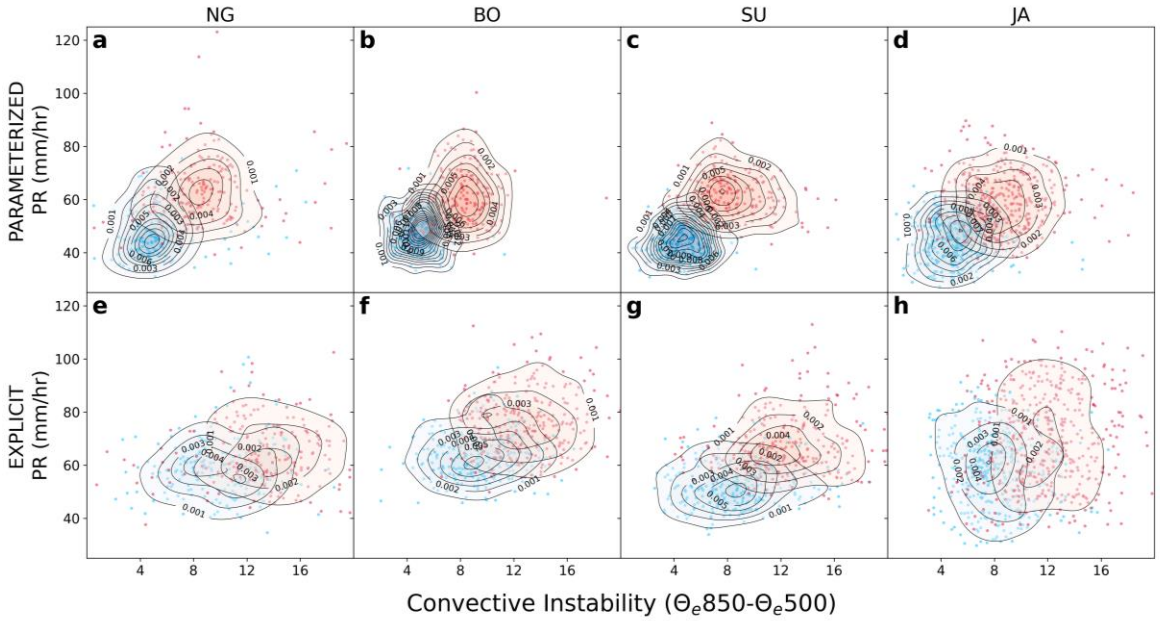

Figure 7: Extreme precipitation events (>99.9th percentile) versus convective instability in different locations for present (blue) and future (red) experiments using convective parameterization (PA, top row) and explicit convection (EX, bottom row). Convective instability is measured as the difference in equivalent potential temperature between the 900-800 hPa and 600-400 hPa layers and averaged over the 12 hours preceding the intense rainfall event. Each dot represents an event in the areas delimited by squares in Fig. 1 and the contours represents the probability estimated using a gaussian Kernel Density Estimator. All present and future point clouds are statistically different from each other using a Fasano-Franceschini test at the 0.01 significance level.

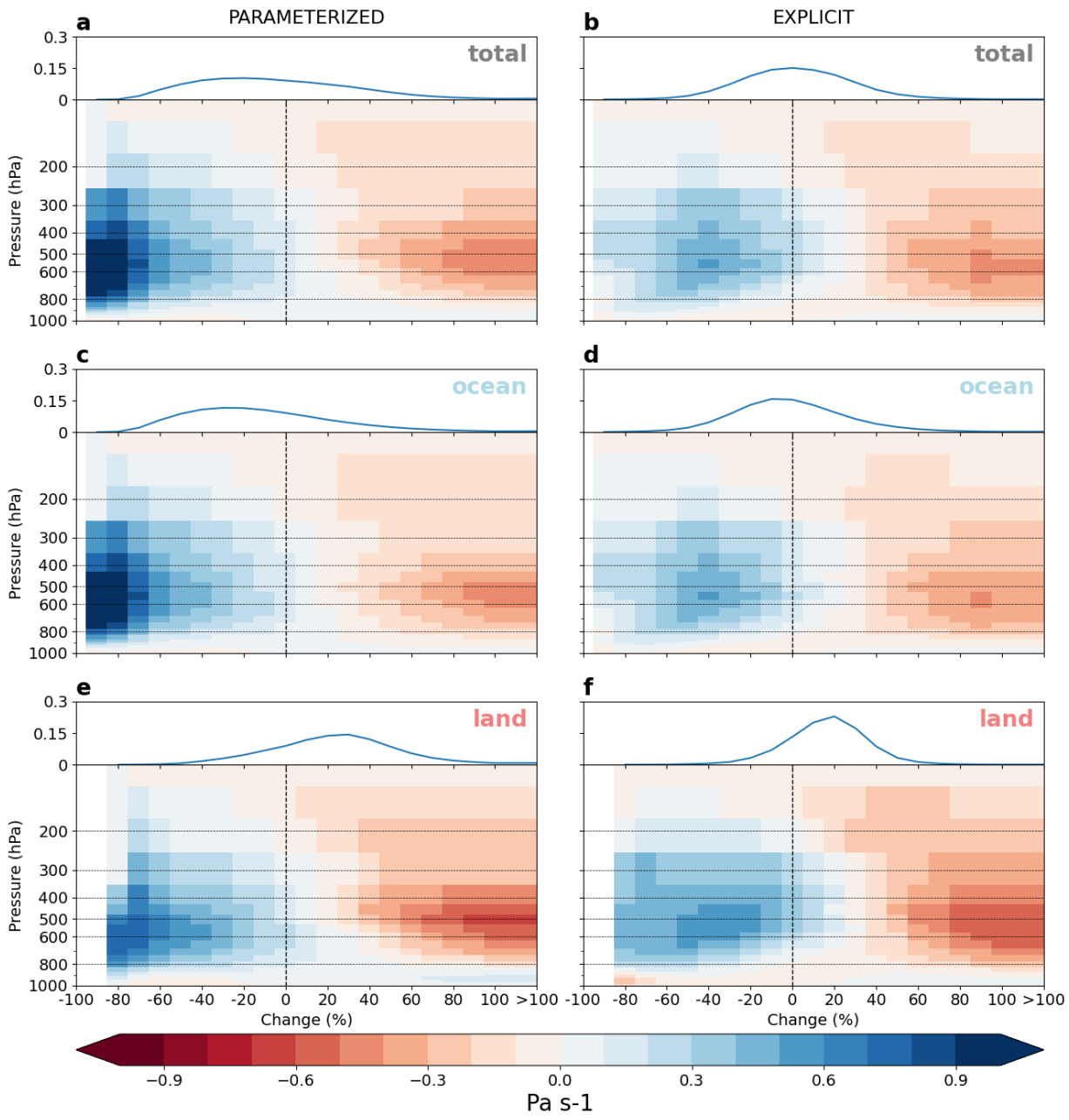

Figure 8: Changes in vertical pressure velocity (ω_e) versus changes in mean precipitation rates of events above the 99th percentile of hourly rainfall averaged over all (a, b), ocean-only (c, d) and land-only (e, f) grid points for the parameterized (left column) and the explicit (right column) convection experiments. Each panel includes a probability distribution of extreme precipitation changes at the top to indicate the most frequent values of changes in the domain.

Figure 1

Click here to access/download

Non-Rendered Figure

Fig1_Domain_csects_and_boxes_new.png

Figure 2

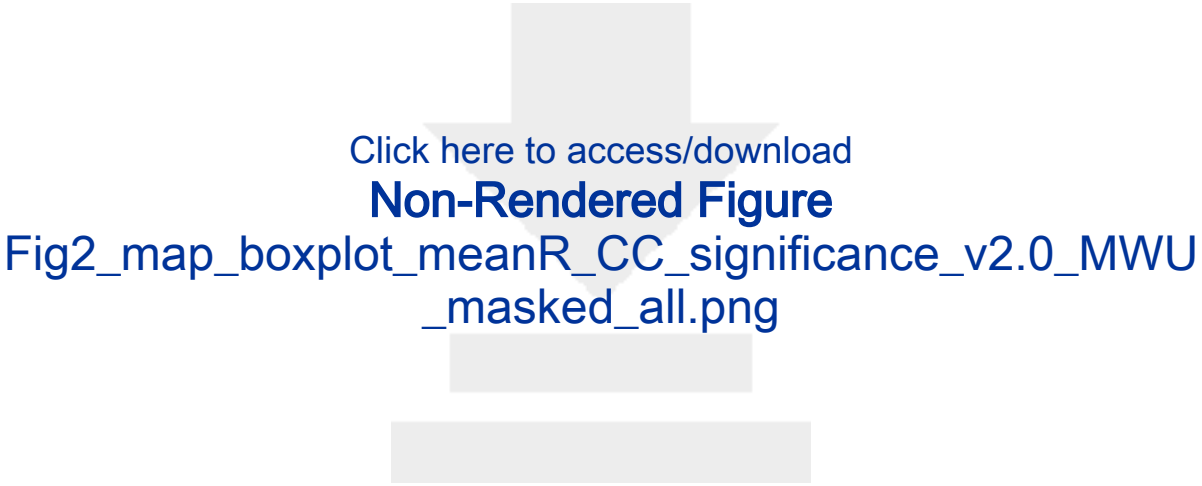

Click here to access/download

Non-Rendered Figure

Fig2_map_boxplot_meanR_CC_significance_v2.0_MWU_masked_all.png

Figure 3

Click here to access/download

Non-Rendered Figure

Fig3_map_masked.png

Figure 4

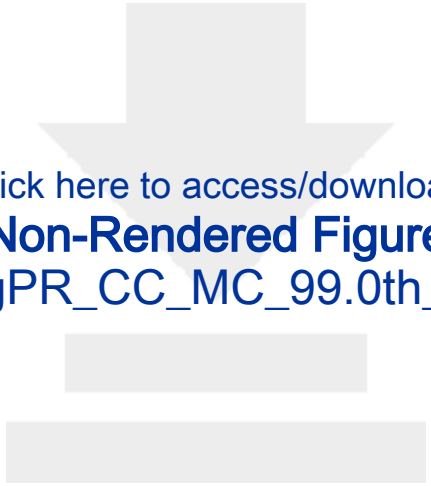

Click here to access/download

Non-Rendered Figure

Fig4_map_scalingPR_CC_MC_99.0th_2013-2016 3.png

Figure 5

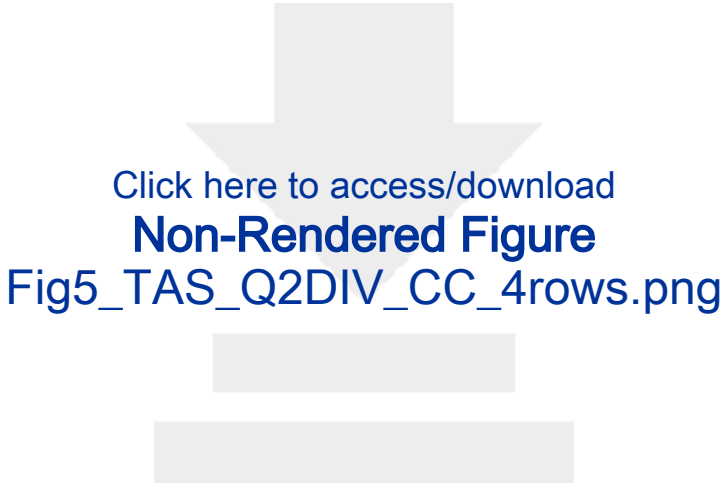

Click here to access/download

Non-Rendered Figure

Fig5_TAS_Q2DIV_CC_4rows.png

Figure 6

Click here to access/download

Non-Rendered Figure

Fig6_vprof_LANDOCEAN_statstabmap_THETAE_CC_plevs.png

Figure 7

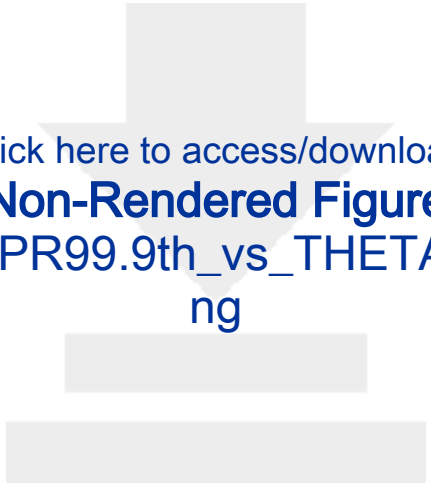

Click here to access/download

Non-Rendered Figure

Fig7_ScatterPlot_PR99.9th_vs_THETAE_0.5_12hours.png

Figure 8

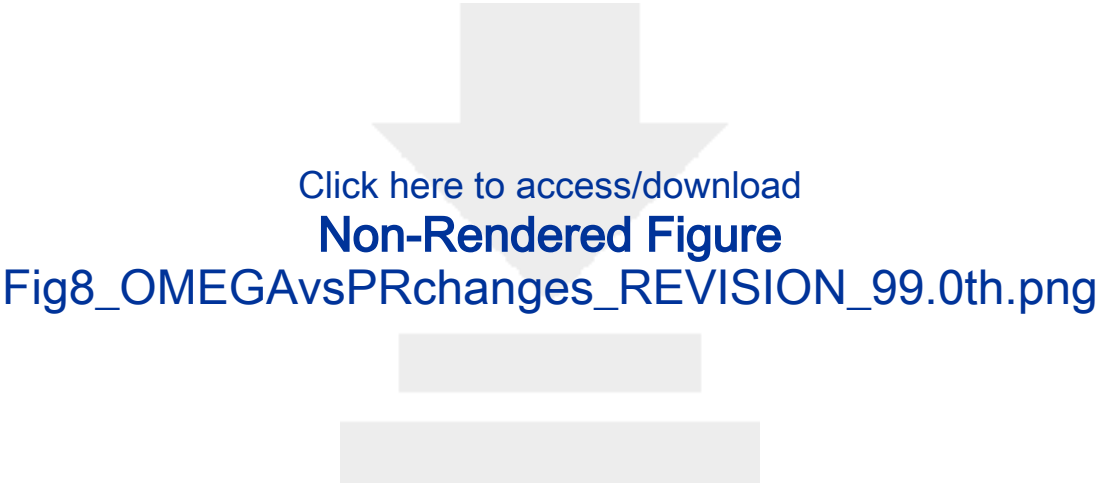

Click here to access/download

Non-Rendered Figure

Fig8_OMEGAvsPRchanges_REVISION_99.0th.png